HHS Public Access

Author manuscript

Prog Retin Eye Res. Author manuscript; available in PMC 2018 March 01.

Published in final edited form as:

Prog Retin Eye Res. 2017 March ; 57: 46–75. doi:10.1016/j.preteyeres.2016.12.002.

Improving our understanding, and detection, of glaucomatous damage: An approach based upon optical coherence tomography (OCT)

Donald C. Hood

Abstract

Although ophthalmologists are becoming increasingly reliant upon optical coherence tomography (OCT), clinicians who care for glaucoma patients are not taking full advantage of the potential of this powerful technology. First, we ask, how would one describe the nature of glaucomatous damage if only OCT scans were available? In particular, a schematic model of glaucomatous damage is developed in section 2, and the nature of glaucomatous damage seen on OCT scans described in the context of this model in section 3. In particular, we illustrate that local thinning of the circumpapillary retinal nerve fiber layer (cpRNFL) around the optic disc can vary in location, depth, and/or width, as well as homogeneity of damage. Second, we seek to better understand the relationship between the thinning of the cpRNFL and the various patterns of sensitivity loss seen on visual fields obtained with standard automated perimetry. In sections 4 and 5, we illustrate why one should expect a wide range of visual field patterns, and iilustrate why they should not be placed into discrete categories. Finally, section 6 describes how the clinician can take better advantage of the information in OCT scans. The approach is summarized in a single-page report, which can be generated from a single wide-field scan. The superiority of this approach, as opposed to the typical reliance on summary metrics, is described.

Keywords

glaucoma; optical coherence tomography; OCT; retinal nerve fiber layer; retinal ganglion cell; macula; visual field

1. Introduction

Glaucoma is a progressive optic neuropathy characterized by specific changes at the optic nerve, and specific patterns of abnormal regions on the visual field (VF). Thus, traditionally most clinicians who care for glaucoma patients base their diagnosis of glaucoma upon both structural and functional [i.e., VF] damage. The assessment of structural damage is often based upon a fundus exam of the optic disc with stereo-photographs of the disc typically obtained for documentation. However, glaucoma specialists show considerable disagreement

Corresponding author: Tel/fax: +1-212-212-222-7934/212-854-3492, dch3@columbia.edu.

in their interpretation of stereo-photographs (Abrams et al. 1994). Recently, clinicians have become increasingly reliant upon computerized imaging technologies, most importantly optical coherence tomography (OCT), to provide information about structural damage and to help in the diagnosis and monitoring of glaucoma.

Despite significant improvements in OCT technology, most clinicians treating glaucoma are not taking advantage of the full potential of OCT. For example, many clinicians only obtain OCT scans of the optic disc. However, without scans that include the macula, glaucomatous damage to this vital region will be missed (Hood et al, 2014c; Wang et al, 2015). Further, clinicians are currently depending heavily upon summary metrics, such as average retinal nerve fiber layer (RNFL) thickness around the disc, or within quadrants or clock hours of the disc. These summary metrics can also miss eyes with clear damage seen on probability maps (Hood et al, 2014c; Wang et al, 2015), which will be described below. In addition, many clinicians do not look at the actual scans, unlike retinal specialists who are trained to closely examine OCT scans and to relate them to the underlying anatomy. In fact, most commercial OCT reports designed for detecting glaucoma either show an image from a circle scan on a scale too small for details to be appreciated or omit these images entirely. As we will illustrate below, there is important information to be gleamed by viewing the fine structure of these images. Finally, these same commercial reports are not, in general, optimally organized to allow the clinician to appreciate the topographical nature of the structural damage, or to help them understand the relationship between this damage and abnormalities seen on VFs. If abnormal regions on structural (OCT) and functional (VF) tests agree, it significantly increases the likelihood of glaucomatous damage, which may decrease the need for repeated testing.

The purpose here is to present an approach that overcomes these problems and thereby improves the usefulness of OCT imaging for understanding and detecting glaucomatous damage. We start by considering the nature of glaucomatous damage as seen on OCT scans. In section 2, a schematic model of glaucomatous damage is developed for this purpose and used as a framework for describing early glaucomatous damage. In sections 4 and 5, we relate the damage seen on OCT scans to the various patterns of sensitivity loss seen on VFs. Finally, section 6 describes how the clinician can take better advantage of the information in OCT scans.

2. A schematic model of glaucomatous damage

To better understand glaucomatous damage to the macula, we previously proposed a schematic model (Hood et al., 2011b; 2012; 2013a). By macula, we meant the central ±8° surrounding fixation. This region contains over 30% of our retinal ganglion cells (RGCs), although it represents less than 2% of the total retinal area (Curcio & Allen, 1990). And by schematic, we meant that the model was a simplified representation and that the actual situation was likely to be more complex, as well as different, in some of the details. Here we extend this schematic model in several ways, including adding a map of the region outside the macula where most of the test locations of the 24-2 VF fall. This schematic model of glaucomatous damage has two classes of assumptions.

2.1. Assumption 1: A map relating locations in the retina to regions around the optic disc

The axons of the RGCs travel in the RNFL in bundles and enter the optic disc. The first assumption of our schematic model relates the locations of the RGCs on the retina to the regions around the optic disc where their axons enter. The schematic model consists of two parts: a detailed map of the macular region (Fig. 1) and an overall map of the retinal regions associated with the temporal half of the disc (Fig. 2). Note: when we say “around or at the disc” or “regions of the disc”, we are, in general, referring to regions of a circle that is 3.4 mm from the center of the disc, as shown in Fig. 1A (dashed circle in right panel). This is, of course, the location of the circumpapillary (cp) RNFL thickness plot.

Our map of the macula (Fig. 1A) relates the superior (magenta) and inferior (light blue) areas of the macula (Fig. 1A, left) to the associated regions of the disc (Fig. 1A, right). While this map was based upon OCT cpRNFL thinning, Hood et al. (2011; 2013a) showed that it was in qualitative agreement with the RNFL bundle tracings described by Jansonius et al. (2009). The faint lines in Fig. 1A are the Jansonius et al. (2012) tracings. Note: all eyes are presented as if they are right eyes throughout this paper, except for Figs. 19 and 23.

Figure 1B shows the relationship between our map in Fig. 1A and the cpRNFL thickness plot, the most common OCT graphical representation of glaucomatous damage. In this plot, the cpRNFL thickness (black, magenta and blue line in Fig. 1B) is shown as a function of location around the disc along a circle 3.4 mm in diameter. The horizontal arrows above the curve in Fig. 1B indicate the regions of the cpRNFL associated with the superior (magenta) and inferior (light blue) areas of the macula.

The cpRNFL thickness plot in Fig. 1B is obtained either directly from a circle scan of the disc or derived from a cube scan, which is comprised of many line scans, of the disc. Figure 1B is referred to as a TSNIT plot because it starts at the temporal most point of the disc (9 o’clock for the right eye, labeled 0° on all figures) and proceeds clockwise from the temporal (T) to superior (S) to nasal (N) to inferior (I) to temporal (T) quadrants. On a TSNIT plot, the nasal portion of the disc is in the center. Thus, the TSNIT plot (Fig. 1B) divides the portion of the disc associated with the macula into two regions; the inferior region, represented by the light blue arrow, is on the right side and the superior region, represented by the magenta arrows, is largely on the left side. However, the superior region is partially on the right side as well because the boundary between the superior and inferior regions does not fall at 0°, as shown in Fig. 1A (right panel). By presenting the nasal half of the disc in the center, the TSNIT plot makes a comparison between RNFL damage and a VF defect more difficult than it needs to be.

For this reason, Hood and Raza (2014) recommended plotting cpRNFL thickness as an ***NSTIN plot*** (Fig. 1C). This plot starts at the nasal most point (3 o’clock for the right eye, labeled ±180°) and travels counterclockwise. Some OCT manufacturers provide the NSTIN plot as an option; others have said they plan to do so. In any case, we will use NSTIN plots for the remainder of this review. On an NSTIN plot, the region of cpRNFL plot associated with the macula is in the center as illustrated by the magenta and blue arrows in Fig. 1C.

To extend our map to include the entire temporal half of the disc, we use the Jansonius et al. (2012) tracings to approximate the retinal area associated with it. In particular, we assume that the blue and red curved lines in Fig. 2A show the approximate course of the RNFL bundles associated with the 12 o'clock (red) and 6 o'clock (blue) locations on the disc. Our schematic model assumes that the axons of the RGCs within the red and blue borders enter the temporal half of the disc. While the borders of our schematic model are based upon traces of RNFL bundles, they show good general agreement with the map proposed by Garway-Heath et al. (2000) derived from RNFL defects seen on fundus photographs. Of course, as they pointed out, there will be variation in this map among individuals. (See also Hood et al., 2007; 2009; Lamparter et al., 2013; Denniss et al., 2012; 2014; Turpin et al., 2015.) While in the future it might be useful to adjust for individual parameters such as fovea-to-disc angle, axial length, and foveal morphology (Knighton and Gregori, 2012; Lamparter et al., 2013; Denniss et al., 2012; 2014; Turpin et al., 2015), the average maps in Figs. 1A and 2B provide a useful approximation for understanding the consequences of damage to different parts of the cpRNFL, as we will see below.

According to this map, the RGC axons entering the temporal half of the disc come from the retinal area within ±15° of the center of the fovea (dashed black circle, Fig. 2A), plus the area of the retina labeled as the "nasal step" in Fig. 2A. We called the latter portion of the retina the "nasal step" because it includes the area associated with the so-called nasal step defects seen on VFs. Again notice that the TSNIT plot in Fig. 2B divides the region associated with the central ±15°+nasal step into two regions. On the other hand, with the NSTIN plot in Fig. 2C, this central portion of the retina is in the center of the plot.

2.2. Assumption 2: The nature and location of damage

2.2.1 The superior and inferior vulnerability zones—The second assumption of the schematic model specifies the relative vulnerability of local disc regions to early glaucomatous damage. Figure 3A shows the vulnerable regions as described by Hood et al. (2013b). They examined the locations of local glaucomatous damage around the optic disc in eyes with 24-2 MD better than -6dB. While local damage was seen in all quadrants, it was most common in the two regions indicated by orange and green arcs in Fig. 3A. The third most common region (gray arc in Fig. 3A) overlapped the superior and nasal quadrant. The area of the retina associated with this gray arc is largely outside the area covered by the most commonly used VF test, the 24-2 test pattern of static automated perimetry (SAP) and will not be considered here. (Note: defects in this gray region should be associated with an "inferior temporal wedge", which could be easily missed by the 24-2 VF, where at most it would include two points nasal to the disc.)

It is generally thought (e.g., Quigley and Green, 1979), that local defects are most often seen in the superior and inferior quadrants. For example, OCT studies typically find that cpRNFL thinning of the superior and inferior quadrants is a more sensitive measure of glaucomatous damage than is thinning of the temporal or nasal quadrants (e.g., Kanamori et al., 2003; Nouri-Mahdavi et al., 2004; Budenz et al., 2005; Medeiros et al., 2005). However, according to Fig. 3A this does not tell the whole story. First, according to Hood et al. (2013b), it is the temporal half of the superior and inferior quadrants (i.e., 45° to 90° and −45° to −90° in Fig.

3A,B) that are particularly vulnerable to early local damage. This is consistent with OCT cpRNFL thickness data suggesting that 6, 7, 11, and 12 are the clock hours of the disc that are most likely to be affected by glaucomatous damage (e.g., Kanamori et al., 2003; Nouri-Mahdavi et al., 2004; Budenz et al., 2005; Medeiros et al., 2005). We will refer to the orange and green regions in Fig. 3A,B as the superior vulnerability zone (SVZ) and inferior vulnerability zone (IVZ), respectively. Second, while the SVZ (orange) and the superior macular region (magenta) do not overlap, the IVZ (green) and the inferior macular region (light blue) do. This region of overlap (black arc in Fig. 3A and black line in Fig. 3B) was called the "macular vulnerability zone" (MVZ) by Hood et al. (2012, 2013a); it is discussed below in section 2.2.3.

2.2.2 Widespread damage—The SVZ and IVZ were identified based upon local damage. However, glaucomatous damage can also be widespread and include large portions of the optic disc, and even the entire disc (e.g., Hoyt et al., 1973; Anderson, 1983; Airaksinen et al., 1984). It is probably safe to say we know less about the relative vulnerability of different regions of the disc to widespread damage, than we do about vulnerability to local damage. For now, we assume that while all regions of the disc are vulnerable to widespread damage, the SVZ and IVZ lose a greater number of axons, perhaps because they have the thickest RNFL when healthy (Hood et al., 2012).

2.2.3 Macular damage and the RGC+ thickness map—Early damage to the macula seen on OCT scans can also be widespread, as well as local (Hood et al, 2014c). Furthermore, OCT analysis based only on cpRNFL thickness can miss both types of macular damage (Hood et al, 2014c; Wang et al, 2015). On the other hand, macular damage is easy to detect with thickness maps of RGC plus inner plexiform (RGC+) layer derived from OCT cube scans of the macula (e.g., Tan et al., 2009; Wang et al., 2009; Hood & Raza, 2011; Mwanza et al., 2011; Hood et al., 2013a; Wang et al., 2015). Thus, cube scans of the macula are essential. [Technical note: Instead of RGC+ thickness, some studies have used either RGC alone or RGC+IPL+RNFL (aka ganglion cell complex). We prefer RGC+ as it is not always possible to see the border between the RGC and inner plexiform layers. In addition, there is more information obtained by generating separate RGC+ and RNFL maps, as will be illustrated in section 3.]

Figure 4 shows the average RGC+ thickness maps of the 54 healthy controls (panel A) and patients with moderate glaucoma (panel B) (Hood et al., 2012; 2013a). These maps were derived from a 6×6mm (about 10° by 10°) sdOCT cube scan centered on the fovea. The RGC+ difference/thinning map is shown in panel C, where the region of greatest RGC+ thinning is shown as dark red. There is greater damage (more thinning) in the inferior retina in Fig. 4C and the schematic model provides an explanation (Hood et al, 2011; 2012; 2013a; Kim et al., 2014; Zhang et al., 2016). The axons of the RGCs in the inferior portion of the inferior macula (i.e., dashed lines within the light blue border in Fig. 4D) enter the disc in the MVZ. Thus, the retinal areas most vulnerable to glaucomatous damage include the area of the macula associated with the MVZ (i.e., the white region within the light blue borders in Fig. 4E), along with the traditional arcuate regions (large Xs in Fig. 4E) entering the SVZ and IVZ. The axons from the rest of the macula (i.e. the maculo-papillary region of the

inferior macula plus the entire superior macula) enter the disc in the temporal region (Fig. 4D). This less vulnerable region of the macula is shown in gray in Fig. 4E.

3. Understanding patterns of glaucomatous damage seen with OCT

Various classification schemes have been proposed to describe the pattern and severity of glaucomatous damage. Some of these schemes focus on classifying patterns of VF loss (e.g., Keltner et al., 2003), while others attempt to provide a basis for staging glaucomatous damage (e.g., Hodapp et al., 1993; Brusini and Filacorda, 2006; Brusini and Johnson, 2007; Susanna and Vessani, 2009). All have one common aspect; they are based upon VFs. Here we take a different approach and focus on patterns of RNFL and RGC+ loss seen on OCT scans. In a sense, we are asking: How would you describe glaucomatous damage if you only had OCT scans?

3.1. Evaluating glaucomatous damage with OCT scans of the disc and macula

Figure 5 illustrates our approach to evaluating the nature of glaucomatous damage using OCT. This analysis is based largely upon two 6×6mm cube scans, one centered on the macula (as in Fig. 4) and one centered on the disc. To obtain a high quality circumpapillary image, an averaged circle scan of the disc is also obtained. (In section 6.4, we illustrate how a single wide-field scan can replace these three scan protocols.)

Thickness maps of the RNFL are obtained from the macular (Fig. 5C, left) and disc (Fig. 5C, right) cube scans, and a thickness map of the RGC+ layer (Fig. 5D) is obtained from the macular cube scan. [Technical note: an RGC+ map around the disc is of limited use given how thin the RGC layer is outside the macula.] The curve in Fig. 5B shows the cpRNFL thickness (NSTIN) plot as in Fig. 2C, derived from the RNFL thickness map (Fig. 5C, right) for a 3.4 mm diameter circle centered on the disc (solid black circle in C). The image in Fig. 5A is from the circle scan, which also has a diameter of 3.4 mm. As will be illustrated below, by inspecting enlarged images of high resolution scans as in Fig. 5A, one can obtain important insights about the nature of the damage. [Technical note: As the cpRNFL thickness plot in Fig. 5B was obtained from the cube scan of the disc, the cpRNFL plot for circle scan image in Fig. 5A may not be in exactly the same place. However, the deviations were very minor for the examples shown here.]

Finally, the thickness maps in Figs. 5C and 5D are turned into probability maps by comparing the patient's thickness values to those of an age-similar healthy control group. The two RNFL probability maps based upon Fig. 5C are combined in Fig. 5E; the RGC+ probability map based upon Fig. 5D is shown in panel F. The color of the probability maps indicates the significance level with a continuous scale from green ($p>0.1$) to dark red ($p<0.001$) with yellow, red and dark red indicating probabilities of 0.05, 0.01 and <0.001, respectively. The black circles in panels E and F have a radius of 8°, which indicates the macular area of the retina.

3.2. Patterns of glaucomatous damage and the schematic model

We begin with the generally accepted assumption that most, if not all, glaucomatous damage starts in the optic disc, not the retina. Whatever the proximal cause [e.g., intraocular pressure

(IOP), vascular, glial], this damage leads to a loss of axons and a thinning of the cpRNFL (Weinreb and Khaw, 2004). Thus, to understand the patterns of glaucomatous damage seen on RFNL and RGC+ probability maps, as well as the pattern of abnormal regions present on VFs (sections 4 and 5), we need to understand the variations in cpRNFL thickness due to glaucoma. Figure 5 can be used to illustrate our approach.

Two relatively local defects can be seen in Fig. 5A,B, one in the superior disc (yellow and black arrows) and one in the inferior disc (white and red arrows). Let's consider the defect in the inferior disc first. This local thinning of the cpRNFL (red arrow in Fig. 5B) can be confirmed on the image from the circle scan in Fig. 5A, where the white arrow indicates the region of very thin RNFL, which is easier to see in the enlarged image of this region (inset to right). The abnormal region (red bar in Fig. 5B) is within the IVZ (green bar in Fig. 5B) and includes the MVZ (black bar). The location of this defect (red arrows) can be confirmed with the RNFL (C) and the RGC+ (D) thickness maps, and especially with the associated probability maps in panels E and F. The RNFL probability map (E) shows a clear inferior arcuate shaped defect impinging on the macula region (circle in E), while the RGC+ probability map (F) indicates local RGC+ thinning within the macula. These probability maps provide a particularly good way to verify the location of the defect, and to some degree, its extent. [Technical note: In Fig, 5, as well as the figures below, the red dashed vertical lines mark the points where the cpRNFL thickness falls into the 1% confidence (red) region. While this offers a quantitatively defensible definition of the cpRNFL "abnormal region", it undoubtedly underestimates the width of the region thinned due to glaucoma. However, because healthy controls have a wide range of cpRNFL thickness, we cannot obtain an absolute measure of the decrease in thickness, unless the affected eye was scanned before damage occurred. If the other eye is healthy with normal cpRNFL thickness, it is sometimes possible to use it to determine the extent of the damage to the cpRNFL due to the high degree of symmetry typically present between eyes of the same individual.]

3.2.1 Defects in the cpRNFL vary in location—Using the schematic model, we can predict the abnormal location(s) on the RGC+ and RNFL probability maps associated with abnormal thinning on the cpRNFL thickness plot, and vice versa. To aid in this comparison, the location of the SVZ (orange), IVZ (green), MVZ (black) and the region associated with the macula (magenta and blue arrow) are shown in Fig. 5B, and the boundary of macular area (±8°) is shown on the RGC+ probability map in Fig. 5E,F as the black circles.

To illustrate the relationship between local thinning of the cpRNFL and the abnormal regions on the probability maps, we generated hypothetical RNFL and RGC+ probability maps associated with 3 deep, and local, RNFL defects within the IVZ. In particular, the 45° wide IVZ was divided into three regions, each 15° in width. The retinal regions associated with these 3 cpRNFL regions were roughly estimated based upon the Jansonius et al. (2012) bundles (Fig. 2A) as shown by the black, blue and green regions in Figs. 6A. (Note that the map implied by Fig. 6A is not based upon a precise anatomical model. Rather Figs. 6–8 are teaching aids to help understand the consequence of different patterns of cpRNFL damage.) Figure 7B–G shows the RNFL and RGC+ probability maps for these 3 hypothetical deep defects. The defect closest to the temporal edge of the IVZ (black region in Fig. 7A) falls within the MVZ. The expected abnormal regions within the associated RNFL (Fig. 7B) and

RGC+ probability maps (Fig. 7E) are shown in red. [Note: the yellow region in Fig. 7F is outside the central ±8° (black circle), but inside the expected region of an abnormal RGC+ layer. This region will not necessarily appear as abnormal on RGC+ probability maps because the RGC layer is very thin outside the macula. The yellow is meant to signify that it may or may not be seen on the RGC+ plot.]

The local deep defect represented by the blue region in Fig. 7A is partially within, and partially outside, the MVZ. The RNFL and RGC+ probabilities (Fig 7C,F) reflect this. Finally, the third defect (green region in Fig. 7A), which is closest to the inferior edge of the IVZ, is completely outside the MVZ. Thus, the RGC+ map (Fig. 7G) is unaffected. The associated RNFL map only shows part of the area of the RNFL affected (red arcuate in Fig. 7D), as most of the affected area (within dashed red borders) falls outside the region of the scan.

Of course, actual data may deviate from these hypothetical results in Fig. 7. Defects are not all deep or local (e.g., Hood et al., 2014c), and the maps in Figs. 1 and 2 will vary among individuals (e.g. Garway-Heath et al., 2000; Hood et al., 2007; 2009; Lamparter et al., 2013; Denniss et al., 2012; 2014; Turpin et al., 2015). However, the schematic model, and Fig. 7, can help understand the general relationship between abnormal thinning on the cpRNFL thickness plot and the RNFL and RGC+ probability maps. For example, consider the defects seen on the cpRNFL plot in Fig. 5B.

The location of the defect in Fig. 5B (red bar) includes most of the black and blue defect regions in Fig. 7A. The location of the abnormal (red) regions on the RNFL and RGC+ probability maps (Fig. 5E,F) are approximately what we would expect from Fig. 7B, C, E and F.

This example also illustrates the asymmetrical mapping of the macula region onto the superior and inferior disc captured in our schematic model (Fig. 3). Consider the local defect in the superior disc (black arrows in Fig. 5). Compared to the inferior defect, it is in about the same location relative to the center of the temporal quadrant (9 o'clock for the right eye). In particular, both the superior and inferior defects start approximately at the edge of the temporal quadrant and extend toward 12 or 6 o'clock. However, as expected from the schematic model (Fig. 3) the damage to the RGC+ layer in Fig. 5F is within the macular region for the inferior defect, but just outside it for the superior defect. This is illustrated in Fig. 8, which is in the same form as Fig. 7, but for 3 hypothetical defects in the SVZ, as shown in Fig. 6B. The region in black in Fig. 8A is in about the same location as the defect in the SVZ in Fig. 5A,B. As expected from the model, the abnormal area on the probability maps (Fig. 5E,F) is outside the macula (Fig. 8D,G). In agreement, Zhang et al. (2016) recently reported that the rim or RNFL defects seen in the superior-temporal sector of the disc in photographs are unlikely to be associated with macular damage; however, defects in the inferior-temporal region are likely to affect the macula.

A close examination of the predicted and actual defects will reveal discrepancies in details. These may be due in part to variations in the map among individuals as mentioned in section 2.1. However, it is probably largely due to the fact that the actual defects are less deep than

the schematic defects. In other words, while the hypothetical defects assume a complete loss of RNFL, the actual abnormally thin regions often show preserved (residual) RNFL. Thus, in addition to location, the abnormal regions identified on the cpRNFL plot can vary in depth of cpRNFL loss.

3.2.2 Defects in the cpRNFL vary in depth—Figure 9B shows a local defect (red arrow and bar) in about the same region of the disc as in Fig. 5. However, in this eye the defect is shallower, as can be seen in the inset in Fig. 9A. There is considerable RNFL tissue remaining (yellow arrow). On the macular RGC+ probability map (Fig. 9F), the defect appears as a local, less extensive abnormal region than in Fig. 5F, although the general location is consistent with the schematic defects in Fig. 7B,E.

3.2.3 Defects in the cpRNFL vary in width—In addition to location and depth, the abnormal regions of the cpRNFL can vary in width. The example in Fig. 10 shows a relatively wide defect that extends in the inferior direction to at least the inferior edge of the IVZ (green bars in panels A and B). The red vertical dashed lines mark the extent of the defect defined by where the cpRNFL plot falls into the 1% region. The affected region contains a deep defect in the MVZ (black bar in Fig. 10B and white arrow in Fig. 10A, inset), as well as regions with RNFL remaining (yellow and orange arrows in Fig. 10A, inset). Further, it is likely that the abnormal region in the superior direction approaches the point (black arrow and black and white vertical dashed line, Fig. 10B) associated with the midline of the macular retinal area. It also probably extends to the black and white vertical dashed line in the inferior direction. Both the RNFL and the RGC+ probability maps (Fig. 10E,F) are abnormal over a wide region, as expected from model (Fig. 7B–G).

3.2.4 Defects in the cpRNFL can show very local variations in depth—Finally, in addition to variations in location, depth and width, a defect can show very local variations in cpRNFL thickness as can be seen in Fig. 10 (white, yellow and orange arrows) and Fig. 9 (white and yellow arrows). In some cases, these variations can be seen on the RNFL thickness map. In other cases, the variations may be very local and the segmentation algorithms may miss them. In these cases, the defect may be visible as a variation in cpRNFL reflectance intensity, not thickness, if a circle scan with good resolution is closely examined. The example in Fig. 11 illustrates this point. There are subtle variations in reflectance intensity within the red rectangle in Fig. 11A. These can be better visualized in panel C, where this portion of the scan is enlarged. The arrows in the lower panel of C indicate regions of relatively less (white) and relatively higher (yellow) reflectance intensity. The OCT instruments algorithm produced the green lines to mark the border of the cpRNFL. According to the algorithm, this region had approximately equal cpRNFL thickness along the region that included the yellow and white arrows in Fig. 11C. [Note: the yellow and white arrows indicate approximately the same location in panels C, D, and E of Fig. 11.] However, these variations in intensity correspond to real differences in the RNFL as confirmed by the image in Fig. 11D obtained with an adaptive optics, scanning laser ophthalmoscope (AO-SLO) (Hood et al., 2015a). While these variations may be hard to distinguish from normal variations in intensity on the OCT circle scan, they sometimes can be better visualized on OCT en-face slab images in Fig. 11E (Hood et al., 2015b). See Hood

et al. (2015b) for explanation of OCT en-face slab images. The AO-SLO results suggest that these variations in reflectance seen on OCT images are probably due to the distribution and density of axons within the cpRNFL cross-sectional image (Chen et al., 2015; Hood et al., 2015a).

3.2.5 The cpRNFL can show widespread damage—So far, we have focused on local defects of the cpRNFL. As mentioned in section 2.2.2, damage can also be widespread and encompass large portions of the disc, including the entire disc in some cases. Figure 12 shows an example of the latter. The cpRNFL appears to be thinner than normal throughout most, if not all, locations around the disc in Fig. 12B. In fact, the cpRNFL thickness appears to be approximately the same thickness everywhere. In a healthy eye, the SVZ and IVZ are thicker than in other regions. Thus, the damage in this eye will be more visible in these regions, as can be seen on the RNFL probability map in Fig. 12E. As discussed below in section 3.3.3, individual eyes can show a combination of early widespread and local damage.

3.3. The schematic model and early glaucomatous damage

In this section, we relate the schematic model to data from a recent study of eyes with early glaucomatous damage, by which we mean eyes with MDs better than -6 dB on the 24-2 VF (Hood et al., 2016). This study included 130 eyes with abnormal discs and/or discs with anomalous size and shape (i.e. tilted, small, myopic). Two glaucoma specialists classified the eyes based upon a commercial OCT cpRNFL report, 24-2 and 10-2 VFs, optic disc stereo-photographs, information from the patients' charts (e.g., maximum IOP, corneal thickness, family history) and a report to be discussed in section 6.4. The specialists agreed in their classification of 102 of these eyes; 57 were classified as glaucomatous and 45 as healthy. Below we will refer to the 102 eyes as the early glaucoma reference group (EGRG). All examples thus far (i.e., Figs. 6, 9, 10, 11, and 12), as well as Figs. 17 and 18 to be presented, are from the 57 abnormal eyes in the EGRG. [Note: the inclusion criteria for our "early glaucoma group" was based upon the commonly used classification scheme that categorizes eyes based upon the MD of the 24-2 VF. As we have previously noted (Hood et al., 2011b; 2012; 2013a; 2014d; Traynis et al, 2014; Wang et al., 2015; Grillo et al., 2016), this group of eyes with MD better than -6dB can have marked macular damage seen on OCT RGC+ probability plots (e.g. Figs 5,9,10,12) and 10-2 VFs. Further, the EGRG is not representative of either a group of healthy individuals or a group of typical patients seen in the clinic. The latter would include patients with moderate, and even severe visual field loss. However, it is a particularly interesting group because it should include eyes with the earliest signs of damage. Further, these eyes will also be among the most challenging to diagnose.]

3.3.1 Early glaucoma involves the IVZ and SVZ—According to our schematic model, early damage typically includes one or both of the two 45° sectors of the cpRNFL thickness plot, which we called the IVZ and SVZ (Fig. 3). In agreement, 55 of the 57 glaucomatous EGRG eyes had damage that included the IVZ and/or SVZ, as seen by abnormal regions (1% level, red region) on the cpRNFL plot. Figures 5, 9, 10, 11, and 12 supply 5 examples from this study. The remaining 2 eyes did have damage in the IVZ, although it was only borderline (5% yellow region) on the cpRNFL plot, but clear on the cpRNFL probability plot.

3.3.2 Early damage to the IVZ is more common and deeper than SVZ damage—Our schematic model, as presented thus far, does not make a prediction about the relative susceptibility of the SVZ and IVZ to damage. However, for the 57 abnormal eyes in the EGRG, damage in the IVZ was about 40% more common than damage in the SVZ. In particular, 48 (84.2%) of the 57 eyes had damage in the IVZ, while 34 eyes (59.7%) had damage in the SVZ. Furthermore, while 23 eyes had only IVZ damage, 9 eyes had only SVZ damage. This is consistent with earlier evidence from OCT suggesting that damage in the inferior quadrant is, on average, more common than damage to the superior quadrant (e.g., Budenz et al., 2005; Medeiros et al., 2005).

This early glaucomatous damage in the IVZ often includes a relatively local region of nearly complete loss of RNFL, as seen in Figs. 6, 10, and 11 (white arrows). In fact, a local region with complete or nearly complete loss was seen in 14 (24.6%) of the 57 eyes. In 13 of these 14 eyes, the region of deep local damage was in the IVZ; only one eye had a similar loss in the SVZ. Interestingly, the temporal portion of the IVZ is also the region most often associated with a disc hemorrhage (Lan et al., 2008).

3.3.3 Early damage can be widespread as well as local—In general, it is harder to document widespread, as opposed to local, damage, because there is a wide range of RNFL and RGC+ thicknesses among healthy individuals. We defined widespread damage based upon a combination of the cpRNFL thickness plot (Fig. 12B) and the RGC+ probability plot (Fig. 12D). In particular, to be considered widespread damage, some part of the SVZ, IVZ and temporal quadrant, as well as some part of both the superior and inferior macula regions, must include an abnormal region. Based upon these criteria, 18 of the 57 eyes had widespread damage. Furthermore, some eyes had widespread damage combined with local deep damage as previously described (Hood et al, 2014c).

On the other hand, 37 eyes had local damage as illustrated in Figs. 6, 9, 10, and 11. The most common pattern was local damage largely in the IVZ. In particular, 24 eyes had damage similar to that seen in Figs. 9, 10, and 11. In any case, it is clear that both local and widespread damage are present in early glaucoma.

3.3.4 Early glaucoma typically involves regions both inside, and outside, of the macula—Based upon OCT macular scans, we previously concluded that the macula is commonly affected in early glaucoma (Hood et al, 2012; 2013a). Data from the EGRG support this conclusion. In particular, 51 of the 57 abnormal eyes (89.5%) had macular damage as seen on the RGC+ and/or RNFL probability maps. However, in general the eyes showed damage both inside and outside of the macula. In particular, 50 (87.7%) of the 57 eyes showed abnormal thinning of the RGC+ layer and/or RNFL in both the macula and perimacular regions.

The schematic model supplies a basis for understanding why both the macular and perimacular damage is common in early glaucoma. First, the SVZ and IVZ regions are only 45° wide, while even the very local defects are typically greater than 20° in width, as seen in Figs. 6 and 9. Furthermore, the MVZ is about 50% of the IVZ, with the rest of the IVZ devoted to the region outside the macula. Thus, for the inferior retina, we should expect local

damage to include both the macular and perimacular regions, as it does in Figs. 5, 9, 10, and 11. Second, recall that 18 eyes had widespread damage, which includes the macula. Therefore, it is not surprising to find that most eyes have both macular and perimacular damage.

4. The schematic model and visual field defects

4.1 Assumption 3: A map relating the locations of visual field test to locations on the retina

To understand the relationship between the patterns of damage seen on OCT scans and the abnormalities seen on VFs, we need to expand the schematic model by adding a third assumption. In particular, we need to assume a map that relates VF test locations to local retinal locations.

Figure 13 shows these VF maps for the 24-2 VF (panel A) and 10-2 VF (panel B). The VF test locations are shown as the black symbols. The test locations close to fixation are adjusted to take into consideration the displacement of RGCs near the fovea based upon the *post mortem* histological study of Drasdo et al. (2007), as previously described (Hood et al, 2010; Raza et al., 2011; Hood & Raza, 2011). [Note: we are not taking into consideration individual differences in the distance, and/or angle, between the fovea and disc. One could adjust for these differences, but in general they appear to have little practical impact (Amini et al., 2014; Hood et al, 2014a; Mwanza et al., 2016; Resch et al., 2016). Perhaps in the future more detailed models (e.g., Knighton and Gregori, 2012; Lamparter et al., 2013; Denniss et al., 2012; 2014; Turpin et al., 2015) will enhance OCT and VF agreement. However, as the examples below will attest, the average map in Fig. 13 suffices for our purposes.]

It is worth pointing out that according to the schematic model, the regions of the retina within the red and blue borders in Fig. 13A are the only regions associated with the temporal half of the disc. In contrast, the RGCs from the regions outside these borders, but within the 24-2 VF (e.g., solid black curved line at the top of Fig. 13A), enter the disc in the nasal half of the disc, which they share with axons coming from RGCs outside the region covered by the 24-2 VF (e.g., dashed black curved line at the top of Fig. 13A).

4.2 Relating defects seen on visual field to damage seen on OCT

To compare defects seen on 24-2 and 10-2 VFs to abnormal regions seen on OCT, we can combine the schematic model with the RNFL and RGC+ probability maps. To illustrate this approach, consider the eye in Fig. 9. The 24-2 VF (Fig. 14A) for this eye is normal. However, the 10-2 VF shows a relatively subtle defect near fixation in the upper VF, within the black border in Fig. 14B.

The VFs for this eye (Fig. 14A,B) are consistent with the OCT probability maps. To make this comparison, the probability maps from Fig. 9E,F are shown in field view in Fig. 14C,D. That is, they are rotated/flipped around the horizontal meridian so that upper VF corresponds to inferior retina and lower VF to the superior retina. The locations of the VF test points from Fig. 13A,B are overlaid on these probability maps in Figs. 14C (24-2 locations) and 14D (10-2 locations). Finally, the region of the abnormal cluster of 10-2

points within the black border in Fig. 14B is indicated on the RGC+ probability map in Fig. 14D. In this eye, the spatial agreement between the 10-2 VF and OCT probability maps is excellent, especially considering the various factors that can obscure this relationship such as inter-subject variability in anatomy and intra-subject variability in VF testing (Hood et al., 2009).

In general, defects near fixation are missed or markedly underestimated with 24-2 VFs (Scheifer et al., 2010; Hood et al, 2011b; Hood et al., 2013; Traynis et al, 2014; Park et al., 2016; Sullivan-Mee et al., 2016). Figure 13C illustrates why. Here the 24-2 VF test points are superimposed upon the average map (color) of RGC+ thinning for eyes with moderate damage from Fig. 5C. On average, most of the damage to the RGCs falls within the central 4 points on the 24-2 VF. This is true, not only in the case of moderate damage, as in Fig. 13, but early damage as well (e.g., see Fig. 6 in Hood et al., 2013). For example, in the case of the eye in Fig. 14, the defect is missed on the 24-2 VF because it is relatively narrow and falls largely between the 24-2 VF points in Fig. 14C.

The eye in Fig. 10B has a wider region of cpRNFL thinning than the eye in Fig. 9B. Thus, we should expect the damage on the 24-2 and 10-2 VFs to be more extensive than in Fig. 14A,B. Figure 15A,B indicates that this is the case. The abnormal region on the 24-2 VF (Fig. 15A) is enclosed within the red border. This border is also shown on the cpRNFL probability map in Fig. 15C. Notice that the abnormal RNFL region in Fig. 15C falls within this red border. Similarly, the abnormal region within the black border on the 10-2 VF (Fig. 15B) is shown on the RGC+ probability map in Fig. 15D. The abnormal RGC+ region in Fig. 15D falls within this black border.

The two eyes in Figs. 14 and 15 have damage associated with regions in the upper VF. Figure 16 shows the comparison of the VFs and OCT for the eye in Fig. 5 with damage in the superior and inferior regions of the disc. In the case of the defects seen on the 10-2 VF (Fig. 16B), the correspondence between the expected location and the actual location on the RGC+ probability map (Fig. 16D) is excellent as seen by the gray and black borders. In agreement with the schematic model, the damage is closer to fixation in the upper VFs (lower retina), in spite of the fact that the cpRNFL damage is approximately in the same relative disc location, as pointed out in section *3.2.1.* The abnormal regions of the RNFL probability map in Fig. 16C are also consistent with the 24-2 VF, although the superior VF defect is not seen as clearly as it is on the RGC+ map, and the inferior VF defect is largely outside the region covered by the scan.

5. Understanding patterns of VF defects based upon cpRNFL damage

5.1 Expect a wide variety of VF defects

As illustrated above, the RNFL defects in the SVZ and IVZ vary in location, depth, and width, as well as homogeneity. Thus, one should expect VF defects seen on a 24-2 VF to show a wide range of patterns. While some VF defects will fit the classic patterns described, for example, by Keltner et al. (2003), others will not. In particular, depending upon the depth and width of the RNFL damage, the 24-2 VF can appear completely normal (Fig. 14A), or show a paracentral (Fig. 16A, upper 24-2 VF), or an arcuate (Fig. 16A, lower 24-2 VF)

defect. Remember, according to our schematic model these classic 24-2 VF patterns, as well as partial arcuate and nasal step defects, are largely associated with damage in relatively small (45°) regions of the disc, the SVZ and IVZ. However, based upon the wide variation in the depth, width and homogeneity of the RNFL damage in these regions, defects that do not fall into a simple classification scheme should also be expected. In fact, we should not be surprised if these “non-standard” defects are relatively common, and in fact they are.

Figure 15, already discussed, provides one example of a “non-traditional” VF. In some aspects, it looks almost like a superior altitudinal defect, which is characterized as severe loss throughout the entire hemifield of the 24-2 VF. Except in this case, there is a region of relatively good vision (gray arrows in Fig. 15A). This region was replicated on a 24-2 VF obtained 6 months later. This VF pattern does not fit the Keltner et al. (2003) scheme. This area of the VF with relatively good sensitivity is typically abnormal even in arcuate and partial arcuate defects, which are less severe than altitudinal defects. On the other hand, the variations in sensitivity on the 24-2 VF are probably related to the variations in cpRNFL damage seen in the abnormal region (i.e., within the red rectangle in Fig. 10A). As seen in Fig. 10A (inset), part of this cpRNFL region shows no sign of RNFL (white arrow), while parts show a markedly thinned RNFL (yellow arrow), and others a near normal, although thinned, RNFL (orange arrow).

Figure 17 provides another example. Based upon the 24-2 VF (panel A), there appear to be two defects. There is one in the maculo-papillary region (black border), which is not typically associated with glaucoma, and a second (red border) that looks like a nasal step, which is extended toward fixation. The OCT data and our schematic model, however, suggest a single defect. In particular, the significantly thinned region of the cpRNFL thickness plot (dashed vertical red lines in Fig. 17F), while the portion that is actually thinned probably extends over the region indicated by the black and white dashed vertical lines and horizontal arrows, and perhaps beyond. Based upon the schematic model, we approximated the retinal regions (dashed red and black contours in Fig. 17C) associated with the abnormally thinned cpRNFL regions in Fig. 17F. The abnormal areas on the 24-2 VF (i.e., those enclosed within the solid red and black boundaries in Fig. 17A) should fall within these dashed borders in Figs. 17C, and they do. In short, what appears as two unusual VF patterns is really one continuous defect of varying degrees of RNFL thinning and associated RGC+ loss.

5.1.1 Early visual field abnormalities near the horizontal meridian and the nasal step—A VF is said to have a nasal step defect when one or two of the most nasal points on the 24-2, above or below the horizontal meridian, are abnormal (Keltner et al., 2003). Figure 18A shows a 24-2 VF with a nasal step above (red border) the horizontal meridian. Based upon our schematic model, the region of local cpRNFL thinning (within the red dashed vertical lines in Fig. 18C,D) is consistent with this 24-2 VF defect as shown by the dashed red border in Fig. 18B, which is based upon Fig. 2A. Notice that although abnormal, the affected region of the cpRNFL is still relatively thick, as seen on the scan in Fig. 18C (yellow arrow). We assume this means that many axons are still present.

Based upon the discussion in Section 5.1, a nasal step is just one example of a 24-2 VF pattern just discussed, namely early defects just above the horizontal meridian as seen, for example, within the red border in Fig. 17A. That is, early damage in the IVZ can produce abnormalities at one or more of the test locations of the 24-2 VF that lie nasal to fixation and just above the horizontal meridian.

Why are early defects on 24-2 VFs seen just above the horizontal meridian, as opposed to throughout the VF region enclosed within the red dashed borders in Figs. 17 and 18? In the case of a narrow defect as in Fig. 18B, the 6° grid of the 24-2 VF may be too coarse to detect the arcuate defect until it becomes wider as it approaches the horizontal meridian. (See, for example, Fig. 7 in Hood et al, 2015b). While this is likely a factor in some defects, such as in Fig. 18B, it does not explain the appearance of the nasal defect within the red border in Fig. 17A. In this case, a larger region of the 24-2 VF (dashed red border in panel C) should be associated with the relatively wide cpRNFL defect (dashed white and black lines with arrows in panel E). However, only the nasal step portion of the 24-2 VF (within red border in panel A) appears abnormal. This problem highlights the need for an understanding of the relationship between cpRNFL damage and patterns of VF loss on a more micro level.

5.1.2 Models of incomplete damage of the cpRNFL—While a complete exploration of this topic is beyond the scope of this review, it is worth briefly mentioning two different hypotheses of the nature of local cpRNFL damage. In both cases, we are assuming a local region in which the cpRNFL is abnormally thin, although some of the RNFL remains.

The first hypothesis assumes that all the cpRNFL loss involves axons from the same local region of the retina. For example, consider two extremes. In one case, all the missing axons come from RGCs in the nasal step region, while in the second case they come from RGCs near the disc. In both cases, the cpRNFL would be thinner than normal, but appear homogeneous with normal reflectance intensity. However, in the first case, the VF should show a nasal step defect and reasonably normal regions closer to the disc, as seen in Fig. 18A. In the second case, the reverse should be true, as seen in Fig. 15A. Figure 9 supplies support for the local hypothesis. The location of the very local cpRNFL defect (white arrow in Fig. 9A, inset) is associated with a more peripheral RGC+ defect in Fig. 9D,F.

The second hypothesis assumes that the cpRNFL loss involves axons from a wide region of the retina due to multiple arcuate defects. The example in Fig. 19A,B shows a cpRNFL with widespread thinning extending over most of the superior, temporal and inferior quadrants. Let’s consider the inferior VF/superior disc. The 24-2 and 10-2 VFs (panels C and D) show total deviation values ranging from −1 to −21 dB. According to our schematic model, the areas within the red and black borders on the VFs (panels C and D), should correspond approximately to the portion of the cpRNFL plot indicated by the red and black dashed lines with arrows in panel B. The cpRNFL plot within the corresponding regions in Fig. 19A resemble that of the first hypothesis; in other words, it is thinned and appears of normal reflectance intensity (see inset to panel A). The en-face images in Fig, 19E,F, however, suggest very local defects. Hoyt et al. (1973) described seeing this type of defect on fundus photos; he referred to the fundus as having a “raked appearance”. These local defects are confirmed on the AO-SLO images in Fig. 19G. According to the second hypothesis,

although this entire region of the RNFL is thinner than normal, there are local regions with more (white arrows) or less (yellow arrows) damage. This results in a number of small arcuate defects superimposed on a generally thinned RNFL. To understand the VF of this eye, consider that the test light of the 24-2 and 10-2 VF is 26 minutes in diameter. The small yellow circle in Fig. 19E shows the test light scaled to size. Given its size, it may fall on a relatively abnormal area, a relatively preserved area, or partially on each. Thus, given the local nature of these arcuate regions of damage, the size of the test light, and normal microsaccades, it is not surprising that there is a range of VF loss.

It should be emphasized that there are other models of local damage to be explored and that improved resolution of OCT scans coupled with AO-SLO imaging should lead to an even better understanding of the relationship between VF defects to cpRNFL damage.

5.1.3 Damage to the inferior retina can result in a nasal step in the lower VF—

There is also what appears to be a nasal step in the lower 24-2 VF within black border in Fig. 18A. However, unlike the upper VF nasal step, there is no indication on the OCT scans of a RNFL defect in Fig. 18B–D. Based upon theoretical (Denniss et al., 2014) and empirical (Gardiner et al., 2004) evidence, others have predicted that this should occur, although they suggest different anatomical bases. In agreement with Denniss et al (2014), the inferior VF nasal step in this eye is probably due the location of the raphe. Using an en-face image to visualize the raphe as shown in Chauhan et al. (2014), we were able to trace the foveal-raphe angle. The average angle for 37 eyes was 2.7° ± 3.4, close to the 1.7° ± 4.9 obtained by Huang et al. (2015). The raphe angle for the eye in Fig. 18 was 9.7°, considerably larger than these values. Figure 18E shows our schematic model with the 24-2 VF locations from Fig. 13A; this model includes an average angle of the raphe of 2.7° (dashed blue and red lines temporal to fovea in Fig. 18E). The thick dashed blue line in Fig. 18E is the location of the raphe in this patient's eye. The 24-2 VF points associated with the nasal step in the lower VF (open squares in Fig. 18E) fall close to, or within, the retinal region (shaded blue) associated with the inferior disc. It appears that the location of the raphe results in the nasal step seen in the lower 24-2 VF, although we cannot rule out a contribution from head torsion and/or eye movements during the VF testing. In any case, this lower VF "defect" is actually due to the same damage in the IVZ that is causing the upper VF defect circled in red in Fig. 18E. Thus, whenever both upper and lower nasal steps are seen on the 24-2 VF, the nasal step in the lower VF should be viewed with suspicion until confirmed with OCT.

5.2 VF total deviation (TD) data can be a better indicator of widespread damage than pattern deviation (PD) data

In general, glaucoma specialists are taught to focus on the pattern deviation (PD) plot on the VF, as opposed to the TD plot. The PD, by essentially removing the mean, corrects for diffuse losses due to cataracts, a small pupil, or a relatively high criterion for saying "I see it". On the other hand, this "correction" will also obscure a true widespread loss due to glaucoma, as point out by Artes et al. (2010) in the case of the widespread damage seen on VFs in the OHTS investigation. As noted above, the OCT results also suggest that widespread damage is relatively common. This creates a problem for the clinician. Namely,

if a patient shows a widespread loss of sensitivity on the TD plot, and a normal PD plot, do we believe the TD plot or the PD plot?

In the case of the macula and 10-2 VFs, we have argued that the OCT should be used to answer this question (Hood al, 2014c). In particular, if the entire RGC+ probability map is diffusely abnormal and the portion of the cpRNFL thickness plot associated with the macula (e.g., the temporal quadrant plus the MVZ) has abnormal or borderline thickness, then we can be reasonably confident that the TD is correct. Using these criteria, 21 of the 57 abnormal eyes of the EGRG showed widespread damage of the macula.

The same logic can be applied to the 24-2 VF, although in this case we cannot rely simply on the RGC+ probability plot because it only includes the macula. On the other hand, the cpRNFL plot and the RNFL probability map can be used to confirm widespread damage seen on the 24-2 TD plot..

5.3 The relationship between structural and functional damage

Many papers about glaucoma start with a statement such as, “Structural damage precedes functional damage seen on 24-2 VFs”. This is at best a misleading oversimplification as discussed in detail by Hood and Kardon (2007). They measured the cpRNFL thickness in two regions of the disc, which are approximately the same as the SVZ and IVZ. By comparing the cpRNFL thickness of these regions to the sensitivity of the associated areas of the retina (Fig. 13A), Hood and Kardon (2007) found that the loss in cpRNFL was linearly related to the loss in sensitivity, when the latter was expressed in linear terms, not dB. [Note: see Malik et al. (2012), as well as Hood & Kardon (2007) for reviews of other evidence of a linear relationship between structure and function. In addition, in the Ocular Hypertension Treatment Study (OHTS), VFs and optic disc photography (Kass et al., 2002) identified a similar number of eyes that converted to open angle glaucoma.]

As Hood and Kardon (2007) pointed out, this does not mean that the *detection* of cpRNFL thickness cannot precede the *detection* of changes on the 24-2 VF, or visa versa. If two structural and functional measures are linearly related, two factors will determine which is detected first. The first is test variability. Damage will be detected first on the less variable test. Second, an individual’s baseline values, when healthy, will also be a determining factor. For example, if an individual has a relatively thick RNFL, but a below average VF sensitivity when healthy, then as glaucoma progresses, the VF is more likely to appear abnormal first. The reverse could be true for an individual with a relatively high sensitivity, but below average RNFL thickness, when healthy.

To be fair, there is some evidence that the linear relationship breaks down in the macula and that structural OCT damage may be seen before VF changes (Raza et al., 2011; Rao et al, 2015; Swanson et al, 2004). However, these studies are hard to interpret as various factors contribute to the variability in these data. For example, TD values are the more appropriate measure for some eyes, while PD values are the more appropriate measure for others (Hood et al., 2014c). Furthermore, macular defects can be relatively narrow and may or may not fall in the same location as the corresponding 10-2 VF defect depending on how well the average map in Fig. 13B describes a particular eye.

6. Lessons for the clinic

6.1 Typical clinical analysis of OCT disc scans will miss glaucomatous damage

While some ophthalmologists routinely order an OCT macular cube scan, most presently do not. In fact, many glaucoma specialists order a single OCT scan, typically a cube or circular scan of the optic disc.

Based upon this scan of the disc, cpRNFL thickness is determined by the instrument's segmentation algorithm and plotted as a function of position around the disc as in Fig. 1B,C. This cpRNFL thickness plot is typically part of a commercial report that also provides the clinician with summary statistics (metrics) for identifying eyes with glaucomatous damage. In particular, many specialists depend upon pie charts showing which quadrants or clock hours of the cpRNFL thickness plot are abnormally thin.

While numerous studies have documented that these metrics show reasonably good sensitivity (e.g. 80%), it is hard to interpret these results. On one hand, because we lack a gold standard/litmus test for glaucoma, some of the "abnormal" eyes may not have glaucomatous damage. Under these conditions, 80% correct may be excellent. On the other hand, the level of sensitivity will be influenced by the degree of damage. For example, if the study only included eyes with severe glaucoma, then 80% would be a poor result. To avoid these problems, we focused on eyes with mild, but confirmed, glaucomatous damage.

In particular, the eyes in our EGRG group discussed above had 24-2 VFs with MD values better than -6db and abnormal and/or anomalous appearing discs (Hood et al, 2016). Thus, this is a challenging group with which to assess OCT metrics, because it neither included eyes with moderate and severe glaucoma, nor healthy eyes with totally normal discs.

We asked: How well can standard OCT metrics identify the 57 abnormal and 45 "healthy" eyes in our EGRG (Muhammad et al, 2016)? The standard OCT metrics included average cpRNFL thickness (T), cpRNFL thickness of the quadrants (Q: one red or one yellow), and cpRNFL thickness of the clock hours (CH: one red or 2 contiguous yellow) of the disc. Table 1 summarizes the results. The quadrant (Q) metric had the best accuracy, 87.3%. However, it missed 9 of the 57 eyes with confirmed glaucoma and classified 6 (13.3%) of the 45 "healthy" eyes as abnormal.

6.2 The need for cube scans of the macula and probability maps

Clearly the standard metrics of the OCT disc scans can miss glaucomatous damage. In addition, the metrics of the 24-2 [MD, PSD, and GHT (glaucoma hemifield test)] did an even poorer job on the same set of eyes (Muhammad et al, 2016). However, the damage in these eyes can be easily identified on the RGC+ and RNFL probability maps described above (Hood et al, 2011; Hood & Raza, 2011; Raza et al, 2011; Hood et al., 2014c; Wang et al, 2015). For example, the local defect in Fig. 9 is clearly seen on the probability maps in Fig. 9E, F. However, for this eye, all 3 OCT metrics in Table 1 were within normal limits on the OCT commercial report. In addition, the MD, PSD, GHT and cluster criteria of the 24-2 VF were all within normal limits. Furthermore, even the MD and PSD of the 10-2 VF were normal; only the cluster criteria (CC) for the 10-2 VF was abnormal.

The message for the clinician is clear. Relying on the conventional OCT metrics of disc scans, even if combined with 24-2 VFs, will miss damage. To reliably detect glaucomatous damage, an OCT cube scan of the macula should be obtained and the RGC+ and RNFL probability maps should be scrutinized. Failure to do so will result in macular damage being missed. Note that most glaucoma classification systems deem an eye as having advanced disease if the central VF (hence, the macula) is affected, even if the remainder of the VF is mildly affected (De Moraes et al., 2016).

6.3 An approach to detecting optic nerve damage

Our approach to detecting glaucomatous damage with OCT scans does not rely on automated metrics, but depends instead on visual evaluation of the cpRNFL plot, as well as the RGC+ and RNFL probability maps. This approach can be summarized in a one-page report (Hood and Raza, 2014). The rationale here is that OCT results should be interpreted following the same systematic principles applied in radiology to evaluate other types of imaging scans.

6.3.1. A one-page report—Figure 20 shows the one-page report for the same eye whose results are presented in Figs. 6 and 16. The report is based upon 2 cube scans, one centered on the disc and one on the macula, plus an averaged circle scan of the disc. Panels A through D of the report in Fig. 20 are the same as panels A through D in Fig. 5; they were described in section 3.1. Panels E and F show the probability maps for the RNFL (E) and RGC+ layer (F) presented in VF view as in Fig. 16C and P16D, respectively. As in Fig. 16C, D, the locations of the 24-2 and 10-2 VF points are superimposed.

In addition, four thin vertical red lines have been added. These vertical lines show the average location of the major blood vessels in healthy controls (Hood and Raza, 2014). The actual location of the BVs can be identified by the shadows they cast on the circle scans. The major arcuate RNFL bundles in the SVZ and IVZ typically travel adjacent to the major superior and inferior temporal arteries and veins. Thus, if the location of these blood vessels, and the associated RNFL bundles, are markedly different from normal, then an acrucate abnormality can appear on the RNFL probability plot, even if the eye is healthy. A comparison of the location of the shadows to the average location of the blood vessels can help avoid false positives. There are a number of other causes for false positives, including, segmentation errors, epiretinal membranes, and variations in the morphology of the foveal pit (Chong and Lee, 2012). However, a discussion of these are beyond the scope here.

6.3.2. The principles behind our one-page report—Our approach is based upon 5 principles (Hood & Raza, 2014). First, as argued above (sections 3.1), to detect glaucomatous damage, in general, and macular damage in particular, a cube scan of the macula is needed (Hood et al, 2011a; Hood & Raza, 2011; Raza et al, 2011; Hood et al., 2014c; Wang et al, 2015). Second, probability maps should be included. Macular damage is easier to detect on the RGC+ probability map (Fig. 20F) from macula cube scans than it is from cpRNFL analyses of optic disc scans. Furthermore, the pattern of RNFL damage can be better discerned on a RNFL probability map (Fig. 20E) based upon both cube scans than it can from the probability map based only upon a cube scan of the disc. Third, when VFs

are available, the VF should be topographically compared to probability maps. Circling the abnormal locations, as shown in Fig. 16, is sufficient. If the data are available, the VF information can be superimposed using the same probability scale associated with the thickness maps (Hood & Raza, 2011, 2014). Figure 21 illustrates this latter approach with data from the 24-2 VF for this eye. [Note: the 24-2 VF probabilities are on a continuous scale as suggested by Wall et al. (2009)]. Fourth, the cpRNFL thickness plot should be displayed as an NSTIN plot to make it easier to interpret, as described in section 2.1. Finally, one should examine an image of the cpRNFL as in panel A of Fig. 20. This image should be large enough, and of sufficient quality, so that details of the glaucomatous damage can be seen, and the accuracy of the segmentation of the RNFL can be assessed. This is the reason we included a circle scan in our protocol.

6.3.3. Validation of the report—The one-page report has been validated in two studies. In the first (Hood et al, 2014b), two of us, experienced in reading the report, judged a group of eyes similar to those in the EGRG. In one condition, we classified each eye as “glaucomatous” or “healthy” based only on the report in Fig. 21. With only the report, we showed better agreement than did three glaucoma specialists who had available fundus photos, 24-2 VFs and commercial OCT RNFL reports. More importantly, based upon a reference standard, our diagnostic accuracy was as good or better than that of the individual glaucoma specialists.

To test the generality of these results, in a second study we trained two fellows and two pre-med students to read the report in Fig. 21 (Hood et al., IOVS 2015;ARVO E-Abstract). They showed better agreement than the 3 glaucoma specialists from the first study. More importantly, based upon a reference standard, their accuracy was 100% (pre-med) 100% (fellow), 97.8%, (pre-med) and 95.7% (fellow) as compared to 100%, 85.1%, and 78.7% for the glaucoma specialists. Thus, without fundus photos, and without a medical school education in the case of two raters, their accuracy was better than two of the three specialists.

6.4 A one-page, wide-field report based upon a single scan

With the recent increase in OCT scanning speed, it is now possible in a single scan to cover a region as large or larger than that covered by the combined cube scans of the macula and disc. Based upon this single wide-field scan, a report similar to the one in Fig. 20 can be generated. Figure 22 provides an example for the same eye as in Fig. 20. However, the commercial report in Fig. 22 is based upon a single wide-field cube scan using a swept-source OCT (Hood et al, 2016). The scan is 9 × 12 mm and has 256 b-scans and 512 a-scans per b-scan. The report is similar to the report in Fig. 20, but instead of 3 scans, it required only one.

The image in Fig. 22A was derived from the cube scan by averaging the pixels within an annulus 3.4 mm in diameter. The annulus has a width of 100 μm to improve the quality of the image through spatial averaging. While the quality of this image is not as good as a circle scan based upon multiple scan images, such as in Fig. 20A, it is sufficient for most purposes. The solid curve in Fig. 22B is the derived cpRNFL thickness plot, similar to the

solid curve in Fig. 20B. Panel C is the RNFL thickness map, equivalent to the two panels in Fig. 20C, and panel D is the RGC+ thickness map for the macula, equivalent to the panel in Fig. 20D. The two probability maps are presented in field view in E and F, which correspond to those in Fig. 20E, F. Finally, panel G does not have a counterpart in Fig. 20; it is the en-face slab image as in Fig. 11E.

6.5 The wide-field report and diagnosing glaucoma

6.5.1 How much information is in the wide-field report?—To what extent can the wide-field report as in Fig. 22 be used to diagnose or screen optic nerve damage without any other information (e.g., VFs, family history, fundus photos)? As a first step toward answering this question, the author was given only the wide-field reports, as in Fig. 22, for the 102 eyes in the EGRG. He judged each eye as healthy (H); probably healthy (PH); if forced to choose then healthy (FC-H); optic neuropathy (ON); probably ON (PON); if forced to choose then optic neuropathy (FC-ON). Note that the eyes were judged as “optic neuropathy (ON)”, not “glaucoma”, as without information from a fundus photo or a rim thickness analysis other optic neuropathies such as ION could have been confused with glaucoma.

The author identified 56 of the 57 glaucomatous eyes as optic neuropathy (i.e., ON, PON or FC-ON), and 44 of the 45 Healthy eyes as healthy (i.e., H, PH or FC-H), for an accuracy of 98.0%. This was far better than the best accuracy for the same eyes based upon metrics from OCT (87.3% for Q), 24-2 VFs (80.4% for PSD or GHT), or 10-2 VFs (80.4% for MD, PSD or cluster criteria). Based upon these results, we concluded that a single, wide-field OCT scan has the information needed to diagnose early glaucoma with excellent sensitivity/specificity. (See Hood et al., 2016 for more details.)

6.5.2 Can we find a single metric for detecting damage based upon the wide-field scan?—We have already argued that single metrics based upon OCT and/or VFs miss too many eyes with glaucomatous damage. Instead we are advocating that the glaucoma specialists should take into consideration all the information available in the report. Because machine learning algorithms also have the potential to take into consideration multiple sources of information, we have begun to explore this approach.

Muhammad et al. (2016) classified the same 102 EGRG eyes as healthy or glaucomatous using a hybrid machine learning technique. This technique used convolutional neural networks (CNN) to extract features from elements of the wide-field report and random forest (RF) classifiers to categorize eyes. The input into the neural network model included the RNFL and RGC+ thickness maps (Fig. 22C, D) and probability maps (Fig. 22E, F) as well as the en-face map (Fig. 22G).

The neural network model had an accuracy of 92.3%, which is better than any of the standard metrics. And, it was based upon a single OCT scan. In addition, an analysis of the eyes misclassified suggests it should be possible to improve the performance of the model. Although more work is needed to improve and validate this method, the results are encouraging.

6.5.3 Look at the b-scan images—The report does not contain all the information that can be useful to the glaucoma specialist. In addition, we routinely obtain a high resolution horizontal line through the fovea and a circle scan of the disc. These are useful for detecting other problems such as ERM, RNFL holes, macular pucker, as well as changes due to outer retinal problems, including AMD and diseases of the receptors. Although in most cases, images derived from the cube scan will do as well, the increased resolution available in averaged b-scans scans can be useful.

In any case, clinicians should scrutinize individual b-scans if there is any suspicion of something unusual. Figure 23 shows the wide-field report of an eye initially thought to have glaucoma. The RNFL probability map (E) suggests optic nerve disease and the RGC+ probability map (F) is consistent with local RGC damage associated with this defect. However, the RGC+ plot is not typically this local, or this deep, in eyes with glaucoma. In addition, the corresponding location on the en-face slab image in panel I (red arrow) has a hyper-reflective region that should raise suspicion. This prompted us to look at the b-scans from the cube scan. Figure 23J shows the b-scan through the hyper-reflective and thinned region (green line) in Fig. 23I. It revealed a local lesion that destroyed all retinal layers including the RGC layer and RNFL.

7. Conclusions and Future Directions

We started with the premise that many clinicians are not taking advantage of the full potential of OCT. For example, macular scans are often not obtained and the interpretation of the OCT scans is too often based only on summary metrics, such as average global or quadrant cpRNFL thickness. To a large extent, this applies to many researchers as well. To improve the use of OCT, we developed an approach to address this problem. This approach requires probability plots of both RNFL and RGC+ layers, as well as the typical cpRNFL plot, and makes use of a schematic model to aid in the interpretation of these OCT data. Finally, the approach was summarized in a one-page report, and the utility of this report was discussed. The success of this approach thus far raises some interesting questions.

7.1. Do we really need functional evidence to diagnose glaucoma?

Traditionally, the glaucoma specialists have based the diagnosis of glaucoma upon structural changes seen on fundus photographs, with VFs typically used as confirmation. Why are VFs typically included in the decision process? The reason is likely due to two factors. First, glaucoma specialists show considerable disagreement in their interpretation of stereo-photographs of the disc (Abrams et al. 1994). Thus, stereo-photographs by themselves are not sufficient. Second, a VF can often reveal a pattern of abnormal regions that is associated with optic nerve damage.

However, with OCT, both the existence and pattern of RNFL damage can be assessed. In particular, a single scan has the potential to replace the VF and the fundus photograph, including stereo-photographs, for most purposes. One could counter by arguing that in some eyes the VF can show damage before it is apparent with OCT. This is true, but only in very few cases. In our group of 57 early/mild glaucoma eyes, there was at most one eye. That is,

less than 2% needed VFs for accurate diagnosis. The percentage would be far smaller for a typical population seen in a clinical practice.

One could also argue that sometimes the functional changes are far more, or far less, serious than suggested by the OCT. Therefore, VFs are needed to manage the patients, although this is open to debate. Further, as we have argued elsewhere, the 24-2 pattern is not optimal for this task (Hood et al., 2013a), and at the very least it needs to be modified in order to detect early damage to the macula (Hood et al., 2014a; Ehrlich et al., 2014; Chen et al., 2015).

In addition, one could also argue that fundus photographs are needed to detect disc hemorrhages, other retinal problems, as well as to distinguish glaucoma from other optic neuropathies. This is only partially true as OCT b-scans through the disc and fovea, as well as en-face slab images and rim thickness analyses should be able to accomplish most, if not all, of these tasks, especially when combined with a fundus exam.

In any case, we are not suggesting at this point that the glaucoma specialists should do away with fundus photos and VF tests. We are, however, suggesting that OCT scans, and probably a fundus exam, could be done first and then the need for fundus photos/stereo-photos and VF tests determined. (Note: with some instruments, fundus photographs can be obtained as part of scan protocol.) Further, we are suggesting that OCT scans, if properly used, may be useful for screening. This raises the question, who should read OCT scans?

7.2 Who should read and interpret OCT scans?

To put this question in perspective, one should keep in mind that the OCT scans have much better resolution than CAT scans and MRI scans and are rich in clinical information. So on one hand, it does not seem “fair” that other specialists have radiologists to read CAT and MRI for them, while the ophthalmologists are on their own when it comes to OCT scans. On the other hand, although further studies are needed to address the type of training needed, our research thus far suggests that individuals can be trained to read the one-page report and diagnose glaucomatous damage with good sensitivity and specificity.

In any case, an argument can be made for providing fellowships devoted in part to specialized OCT training for at least a subset of glaucoma specialists. They in turn could aid their colleagues in the interpreting particularly difficult OCT scans. At the very least, glaucoma training programs should spend as much time teaching how to read OCT scans as they spent teaching how to evaluate disc photos and VFs.

Further, our recent data suggest that for screening purposes a reading center could be used to assess OCT scans for possible optic neuropathies, including glaucoma.

7.3 Staging glaucoma

As mentioned in section 3.0, nearly all systems for staging glaucoma are based upon the 24-2 VF, including coding for billing in the USA. Consider the eye in Fig. 14 with the normal 24-2 VF, but with a clear defect near fixation as seen on the 10-2 VF and OCT scan. The USA ICD-10 billing codes would classify the eye as “mild or early” based upon the 24-2 VF. However, if this loss was picked up within the central 5° on the 24-2 VF, it would

be classified as “advanced, late, severe”. Staging systems need to include information from OCT macular cube scans and/or 10-2 VFs.

7.4 Evaluating structure versus function

The relationship between structural and functional glaucomatous damage is better than the literature suggests. Many studies have examined the correlation between local structural (i.e., RGC or RNFL thickness) and local functional damage (i.e., 24-2 or 10-2 VF loss). In general, they all find that these correlations are weak to moderate. There are many reasons for this (Hood et al., 2009). In any case, these studies can obscure the underlying agreement between structure and function. Consider, for example, a local defect that appears on both the RGC+ probability map and the 10-2 VF. To compare these defects, the correlation studies need to assume a map between RGC and VF locations. If the individual’s map does not match the average map, the mathematical correlation will be poor. However, the agreement from a clinical perspective may be excellent. In short, there is a need to reconsider how we evaluate the agreement between OCT and VF data, perhaps with a more qualitative approach as suggested in section 5 and/or by focusing on the regions with the largest cpRNFL defect as recently suggested by Ballae Ganeshrao et al. (2015).

7.5 Future directions

OCT technology is changing the practice of ophthalmology and these changes will continue. First, existing OCT technology will continue to show marginal improvements in resolution as light sources, scanning speed and software improve. This improved resolution will lead to better understanding of the nature of local glaucomatous damage as discussed in section 5.1.2. Further, interactive software is already being developed to allow the glaucoma specialist to move from summary metrics to viewing local damage. Second, some believe that a combination of AO and OCT may soon allow us to see individual ganglion cells. Finally, if these attempts are combined with some type of metabolic marker we will at last be able to identify “sick” RGCs in humans, *in vivo*.

Acknowledgments

Many individuals have contributed to the work presented here. Nearly all the patients tested in our laboratory were referred by Dr. Robert Ritch, who is also responsible for first alerting me to early macular damage. He along with Drs. Gustavo de Moraes and Jeffrey Odel have been involved in this work from the beginning. Drs. Dana Blumberg and Jeff Liebmann were key contributors to the EGRG study and along with Drs. Odel, de Moraes and Ritch have worked hard to try to keep our work clinically relevant. In addition, Ali Raza, Nicole De Cuir, Dr. Mindy Jarukasetphon, Dr. Paula Alhadeff and many other students and fellows in the laboratory made important contributions. Further, Daiyan Xin expertly supervised nearly all the OCT testing. Finally, the students in my laboratory during the summer of 2016 suffered through, and helped to correct, earlier versions of this manuscript. Finally, four anonymous reviewers contributed valuable comments that substantially improved the clarity of the arguments.

Abbreviations

cpRNFL	circumpapillary retinal nerve fiber layer
GHT	glaucoma hemifield test
IOP	intraocular pressure

IPL	inner plexiform layer
MD	mean deviation
IVZ	inferior vulnerability zone
MVZ	macular vulnerability zone
NSTIN	nasal, superior, temporal, inferior, nasal
OCT	optical coherence tomography
PSD	pattern standard deviation
RGC	retinal ganglion cell
RGC+	retinal ganglion cell plus inner plexiform layer
RNFL	retinal nerve fiber layer
SVZ	superior vulnerability zone
TSNIT	temporal, superior, nasal, inferior, temporal
VF	visual field

References

Abrams LS, Scott IU, Spaeth GL, Quigley HA, Varma R. Agreement among optometrists, ophthalmologists, and residents in evaluating the optic disc for glaucoma. Ophthalmology. 1994; 101:1662–1667. [PubMed: 7936564]

Airaksinen PJ, Drance SM, Douglas GR, Mawson DK, Nieminen H. Diffuse and localized nerve fiber loss in glaucoma. Am J Ophthalmol. 1984; 98:566–571. [PubMed: 6496612]

Amini N, Nowroozizadeh S, Cirineo N, Henry S, Chang T, Chou T, Coleman AL, Caprioli J, Nouri-Mahdavi K. Influence of the disc-fovea angle on limits of RNFL variability and glaucoma discrimination. Invest Ophthalmol Vis Sci. 2014; 55:7332–7342. [PubMed: 25301880]

Anderson DR. What happens to the optic disc and retina in glaucoma? Ophthalmology. 1983; 90:766–770. [PubMed: 6622014]

Artes PH, Chauhan BC, Keltner JL, Cello KE, et al. Ocular Hypertension Treatment Study Group. Longitudinal and cross-sectional analyses of visual field progression in participants of the Ocular Hypertension Treatment Study. Arch Ophthalmol. 2010; 128:1528–1532. [PubMed: 21149774]

Ballae Ganeshrao S, Turpin A, Denniss J, McKendrick AM. Enhancing structure-function correlations in glaucoma with customized spatial mapping. Ophthalmol. 2015; 122:1695–1705.

Brusini P, Filacorda S. Enhanced glaucoma staging system (GSS 2) for classifying functional damage in glaucoma. J Glaucoma. 2006; 15:40–46. [PubMed: 16378017]

Brusini P, Johnson CA. Staging functional damage in glaucoma: review of different classification methods. Surv Ophthalmol. 2007; 52:156–179. [PubMed: 17355855]

Budenz DL, Michael A, Chang RT, McSoley J, Katz J. Sensitivity and specificity of the Stratus OCT for perimetric glaucoma. Ophthalmology. 2005; 112:3–9. [PubMed: 15629813]

Chauhan BC, Sharpe GP, Hutchison DM. Imaging of the temporal raphe with optical coherence tomography. Ophthalmology. 2014; 121:2287–2288. [PubMed: 25156139]

Chen M, Chui TY, Alhadeff PA, Rosen RB, Ritch R, Dubra A, Hood DC. Adaptive optics imaging of healthy and abnormal regions of retinal nerve fiber bundles of patients with glaucoma. Invest Ophthalmol Vis Sci. 2015; 56:674–681. [PubMed: 25574048]

Chen S, McKendrick AM, Turpin A. Choosing two points to add to the 24-2 pattern to better describe macular visual field damage due to glaucoma. Br J Ophthalmol. 2015; 99:1236–1239. [PubMed: 25802251]

Chong GT, Lee RK. Glaucoma versus red disease: imaging and glaucoma diagnosis. Curr Opin Ophthalmol. 2012; 23:79–88. [PubMed: 22262083]

Curcio CA, Allen KA. Topography of ganglion cells in human retina. J Comp Neurol. 1990; 300:5–25. [PubMed: 2229487]

Denniss J, McKendrick AM, Turpin A. An anatomically customizable computational model relating the visual field to the optic nerve head in individual eyes. Invest Ophthalmol Vis Sci. 2012; 53:6981–6990. [PubMed: 22969077]

Denniss J, Turpin A, Tanabe F, Matsumoto C, McKendrick AM. Structure-function mapping: variability and conviction in tracing retinal nerve fiber bundles and comparison to a computational model. Invest Ophthalmol Vis Sci. 2014; 55:728–736. [PubMed: 24425849]

de Moraes CG, Liebmann JM, Medeiros FA, Weinreb RN. Management of advanced glaucoma: characterization and monitoring. Surv Ophthalmol. 2016; 61:597–615. [PubMed: 27018149]

Drasdo N, Millican CL, Katholi CR, Curcio CA. The length of Henle fibers in the human retina and a model of ganglion receptive field density in the visual field. Vis Res. 2007; 47:2901e2911. [PubMed: 17320143]

Ehrlich AC, Raza AS, Ritch R, Hood DC. Modifying the conventional visual field test pattern to improve the detection of early glaucomatous defects in the central 10°. Trans Vis Sci Tech. 2014 Dec 17.3(6):6. eCollection.

Gardiner SK, Crabb DP, Fitzke FW, Hitchings RA. Reducing noise in suspected glaucomatous visual fields by using a new spatial filter. Vis Res. 2004; 44:839–848. [PubMed: 14967209]

Garway-Heath DF, Poinoosawmy D, Fitzke FW, Hitchings RA. Mapping the visual field to the optic disc in normal tension glaucoma eyes. Ophthalmology. 2000; 107:1809–1815. [PubMed: 11013178]

Goldbaum MH, Jang GJ, Bowd C, Hao J, Zangwill LM, Liebmann J, Girkin C, Jung TP, Weinreb RN, Sample PA. SAP glaucomatous change can occur as deepening of an existing defect and/or its expansion. Trans Am Ophthalmol Soc. 2009; 107:136–144. [PubMed: 20126490]

Grillo LM, Wang DL, Ramachandran R, Ehrlich AC, De Moraes CG, Ritch R, Hood DC. The 24-2 visual field test misses central macular damage confirmed by the 10-2 visual field test and optical coherence tomography. Trans Vis Sci Tech. 2016 Apr 14.5(2):15. eCollection.

Hodapp, E., Parrish, RK., II, Anderson, DR. Clinical decisions in glaucoma. St. Louis: The C.V. Mosby Comp; 1993. p. 52-61.

Hood DC, Anderson SC, Wall M, Kardon RH. Structure versus function in glaucoma: An application of a linear model. Invest Ophthalmol Vis Sci. 2007; 48:3662–3668. [PubMed: 17652736]

Hood DC, Kardon RH. A framework for comparing structural and functional measures of glaucomatous damage. Prog Ret Eye Res. 2007; 26:688–710.

Hood DC, Anderson SC, Wall M, Raza AS, Kardon RH. A test of a linear model of glaucomatous structure-function loss reveals sources of variability in retinal nerve fiber and visual field measurements. Invest Ophthalmol Vis Sci. 2009; 127:875–881.

Hood DC, Raza AS. Method for comparing visual field defects to local RNFL and RGC damage seen on frequency domain OCT in patients with glaucoma. Biomed Opt Exp. 2011a; 2:1097–1105.

Hood DC, Raza AS, de Moraes CGV, Odel JG, Greenstein VC, Liebmann JM, Ritch R. Initial arcuate defects within the central 10 degrees in glaucoma. Invest Ophthalmol Vis Sci. 2011b; 52:940–946. [PubMed: 20881293]

Hood DC, Raza AS, de Moraes CGV, Johnson CA, Liebmann JM, Ritch R. The nature of macular damage in glaucoma as revealed by averaging optical coherence tomography data. Trans Vis Sci Tech. 2012; 1:1–15.

Hood DC, Raza AS, de Moraes CGV, Liebmann JM, Ritch R. Glaucomatous damage of the macula. Prog Ret Eye Res. 2013a; 32:1–21.

Hood DC, Wang DL, Raza AS, de Moraes CG, Liebmann JM, Ritch R. The locations of circumpapillary glaucomatous defects seen on frequency-domain OCT scans. Invest Ophthalmol Vis Sci. 2013b; 54:7338–7343. [PubMed: 24135758]

Hood DC, Nguyen M, Ehrlich AC, Raza AS, Sliesoraityte I, De Moraes CG, Ritch R, Schiefer U. A test of a model of glaucomatous damage of the macula with high-density perimetry: Implications for the locations of visual field test points. Trans Vis Sci Tech. 2014a Jun 19.3(3):5. eCollection.

Hood DC, Raza AS, De Moraes CG, Alhadeff PA, Idiga J, Blumberg DM, Liebmann JM, Ritch R. Evaluation of a one-page report to aid in detecting glaucomatous damage. Trans Vis Sci Tech. 2014b Dec 17.3(6):8. eCollection.

Hood DC, Raza AS. On improving the use of OCT imaging for detecting glaucomatous damage. Br J Ophthalmol. 2014c; 98(Suppl 2):ii1–9. [PubMed: 24934219]

Hood DC, Slobodnick A, Raza AS, De Moraes CG, Teng CC, Ritch R. Early glaucoma involves both deep local, and shallow widespread, retinal nerve fiber damage of the macular region. Invest Ophthalmol Vis Sci. 2014d; 55:632–649. [PubMed: 24370831]

Hood DC, Chen MF, Lee D, Epstein B, Alhadeff P, Rosen RB, Ritch R, Dubra A, Chun TYP. Confocal adaptive optics imaging of peripapillary nerve fiber bundles: Implications for glaucomatous damage. Trans Vis Sci Tech (4). 2015a Apr.10(2):12. eCollection.

Hood DC, Fortune B, Mavrommatis MA, Reynaud J, Ramachandran R, Ritch R, Rosen RB, Muhammad H, Dubra A, Chui TY. Details of glaucomatous damage are better seen on OCT en face images than on OCT retinal nerve fiber layer thickness maps. Invest Ophthalmol Vis Sci. 2015b; 56:6208–6216. [PubMed: 26426403]

Hood DC, De Cuir N, Blumberg DM, Liebmann JM, Jarukasetphon R, Ritch R, De Moraes CG. A single wide-field OCT protocol can provide compelling information for the diagnosis of early glaucoma. Trans Vis Sci Tech. 2016 in press.

Hoyt WF, Frisén L, Newman NM. Fundoscopy of nerve fiber layer defects in glaucoma. Invest Ophthalmol. 1973; 12:814–829. [PubMed: 4752920]

Huang G, Luo T, Gast TJ, Burns SA, Malinovsky VE, Swanson WH. Imaging glaucomatous damage across the temporal raphe. Invest Ophthalmol Vis Sci. 2015; 56:3496–3504. [PubMed: 26047040]

Jansonius NM, Nevalainen J, Selig B, Zangwill LM, Sample PA, Budde WM, Jonas JB, Lagrèze WA, Airaksinen PJ, Vonthein R, Levin LA, Paetzold J, Schiefer U. A mathematical description of nerve fiber bundle trajectories and their variability in the human retina. Vis Res. 2009; 49:2157e2163. [PubMed: 19539641]

Jansonius NM, Schiefer J, Nevalainen J, Paetzold J, Schiefer U. A mathematical model for describing the retinal nerve fiber bundle trajectories in the human eye: average course, variability, and influence of refraction, optic disc size and optic disc position. Exp Eye Res. 2012; 105:70–78. [PubMed: 23099334]

Kanamori A, Nakamura M, Escano MF, Seya R, Maeda H, Negi A. Evaluation of the glaucomatous damage on retinal nerve fiber layer thickness measured by optical coherence tomography. Am J Ophthalmol. 2003; 135:513–520. [PubMed: 12654369]

Kass MA, Heuer DK, Higginbotham EJ, Johnson CA, Keltner JL, Miller JP, Parrish RK 2nd, Wilson MR, Gordon MO. The Ocular Hypertension Treatment Study: a randomized trial determines that topical ocular hypotensive medication delays or prevents the onset of primary open-angle glaucoma. Arch Ophthalmol. 2002; 120:701–713. [PubMed: 12049574]

Keltner JL, Johnson CA, Cello KE, Edwards MA, Bandermann SE, Kass MA, Gordon MO. Classification of visual field abnormalities in the ocular hypertension treatment study. Arch Ophthalmol. 2003; 121:643–650. [PubMed: 12742841]

Knighton RW, Gregori G. The shape of the ganglion cell plus inner plexiform layers of the normal human macula. Invest Ophthalmol Vis Sci. 2012; 53:7412–7420. [PubMed: 23033389]

Kim KE, Park KH, Yoo BW, Jeoung JW, Kim DM, Kim HC. Topographic localization of macular retinal ganglion cell loss associated with localized peripapillary retinal nerve fiber layer defect. Invest Ophthalmol Vis Sci. 2014; 55:3501–3508. [PubMed: 24801510]

Lamparter J, Russell RA, Zhu H, et al. The influence of intersubject variability in ocular anatomical variables on the mapping of retinal locations to the retinal nerve fiber layer and optic nerve head. Invest Ophthalmol Vis Sci. 2013; 54:6074–6082. [PubMed: 23882689]

Lan YW, Wang IJ, Hsiao YC, Sun FJ, Hsieh JW. Characteristics of disc hemorrhage in primary angle-closure glaucoma. Ophthalmology. 2008; 115:1328–1333. [PubMed: 18187197]

Malik R, Swanson WH, Garway-Heath DF. The 'structure-function' relationship in glaucoma: past thinking and current concepts. Clin Experiment Ophthalmol. 2012; 40:369–380. [PubMed: 22339936]

Medeiros FA, Zangwill LM, Bowd C, Vessani RM, Susanna R Jr, Weinreb RN. Evaluation of retinal nerve fiber layer, optic nerve head, and macular thickness measurements for glaucoma detection using optical coherence tomography. Am J Ophthalmol. 2005; 139:44–55. [PubMed: 15652827]

Muhammad, et al. Hybrid deep learning and a single wide-field OCT scan accurately classifies glaucoma suspects. In preparation.

Mwanza JC, Oakley JD, Budenz DL, Chang RT, Knight OJ, Feuer WJ. Macular ganglion cell–inner plexiform layer: Automated detection and thickness reproducibility with spectral domain–optical coherence tomography in glaucoma. Invest Ophthalmol Vis Sci. 2011; 52:8323–8329. [PubMed: 21917932]

Mwanza JC, Lee G, Budenz DL. Effect of adjusting retinal nerve fiber layer profile to fovea-disc angle axis on the thickness and glaucoma diagnostic performance. Am J Ophthalmol. 2016; 161:12–21. [PubMed: 26387935]

Nouri-Mahdavi K, Hoffman D, Tannenbaum DP, Law SK, Caprioli J. Identifying early glaucoma with optical coherence tomography. Am J Ophthalmol. 2004; 137:228–235. [PubMed: 14962410]

Park HY, Hwang BE, Shin HY, Park CK. Clinical cues to predict the presence of parafoveal scotoma on Humphrey 10-2 visual field using a Humphrey Visual Field. Am J Ophthalmol. 2016; 161:150–159. [PubMed: 26476213]

Quigley HA, Green WR. The histology of human glaucoma cupping and optic nerve damage: clinicopathologic correlation in 21 eyes. Ophthalmology. 1979; 86:1803–1827. [PubMed: 553256]

Rao HL, Qasim M, Hussain RS, Januwada M, Pillutla LN, Begum VU, Chaitanya A, Senthil S, Garudadri CS. Structure-function relationship in glaucoma using ganglion cell-inner plexiform layer thickness measurements. Invest Ophthalmol Vis Sci. 2015; 56:3883–3888. [PubMed: 26070060]

Raza AS, Cho JS, de Moraes CGV, Wang M, Zhang X, Kardon RH, Liebmann JM, Ritch R, Hood DC. Retinal ganglion cell layer thickness and local visual field sensitivity in glaucoma. Archives of Ophthalmology. 2011; 129:1529–36. [PubMed: 22159673]

Resch H, Pereira I, Hienert J, Weber S, Holzer S, Kiss B, Fischer G, Vass C. Influence of disc-fovea angle and retinal blood vessels on interindividual variability of circumpapillary retinal nerve fibre layer. Br J Ophthalmol. 2016; 100:531–536. [PubMed: 26269535]

Susanna R Jr, Vessani RM. Staging glaucoma patient: why and how? Open Ophthalmol J. 2009; 3:59–64. [PubMed: 19834563]

Schiefer U, Papageorgiou E, Sample PA, Pascual JP, Selig B, Krapp E, Paetzold J. Spatial pattern of glaucomatous visual field loss obtained with regionally condensed stimulus arrangements. Invest Ophthalmol Vis Sci. 2010; 51:5685–5689. [PubMed: 20538998]

Sullivan-Mee M, Tran MTK, Pensyl D, Tsan G, Katiyar S. Prevalence, features and severity of glaucomatous visual field loss measured with the 10-2 achromatic threshold visual field test. Am J Ophthalmol. 2016; 168:41–50.

Swanson WH, Felius J, Pan F. Perimetric defects and ganglion cell damage: interpreting linear relations using a two-stage neural model. Invest Ophthalmol Vis Sci. 2004; 45:466–472. [PubMed: 14744886]

Tan O, Chopra V, Lu AT, Schuman JS, Ishikawa H, Wollstein G, Varma R, Huang D. Detection of macular ganglion cell loss in glaucoma by Fourier-domain optical coherence tomography. Ophthalmology. 2009; 116:2305–2314. [PubMed: 19744726]

Traynis I, de Moraes CG, Raza AS, Liebmann JM, Ritch R, Hood DC. The prevalence and nature of early glaucomatous defects in the central 10° of the visual field. JAMA Ophthalmol. 2014; 132:291–297. [PubMed: 24407153]

Turpin A, Chen S, Sepulveda JA, McKendrick AM. Customizing structure-function displacements in the macula for individual differences. Invest Ophthalmol Vis Sci. 2015; 56:5984–5989. [PubMed: 26393464]

Wall M, Johnson CA, Kardon RH, Crabb DP. Use of a continuous probability scale to display visual field damage. Arch Ophthalmoly. 2009; 127:749–756.

Wang DL, Raza AS, de Moraes CG, Chen M, Alhadeff P, Jarukatsetphorn R, Ritch R, Hood DC. Central glaucomatous damage of the macula can be overlooked by conventional OCT retinal nerve fiber layer thickness analyses. Trans Vis Sci Tech (4). 2015 Nov 30.(6):4. eCollection.

Wang M, Hood DC, Cho JS, Ghadiali Q, De Moraes GV, Zhang X, Ritch R, Liebmann JM. Measurement of local retinal ganglion cell layer thickness in patients with glaucoma using frequency-domain optical coherence tomography. Arch Ophthalmol. 2009; 127:875–881. [PubMed: 19597108]

Weinreb, RN., Garway-Heath, T., Leung, C., Liebmann, J., Medeiros, F. World Glaucoma Association. [accessed 01.09.16] Consensus 10: Diagnosis of primary open angle glaucoma. 2016. http://www.worldglaucoma.org/consensus-10-preliminary-report/

Weinreb RN, Khaw PT. Primary open-angle glaucoma. The Lancet. 2004; 363:1711–1720.

Zhang C, Tatham AJ, Abe RY, Hammel N, Belghith A, Weinreb RN, Medeiros FA, Liebmann JM, Girkin CA, Zangwill LM. Macular ganglion cell inner plexiform layer thickness in glaucomatous eyes with localized retinal nerve fiber layer defects. PLoS One (11). 2016 Aug 18.(8):e0160549. [PubMed: 27537107]

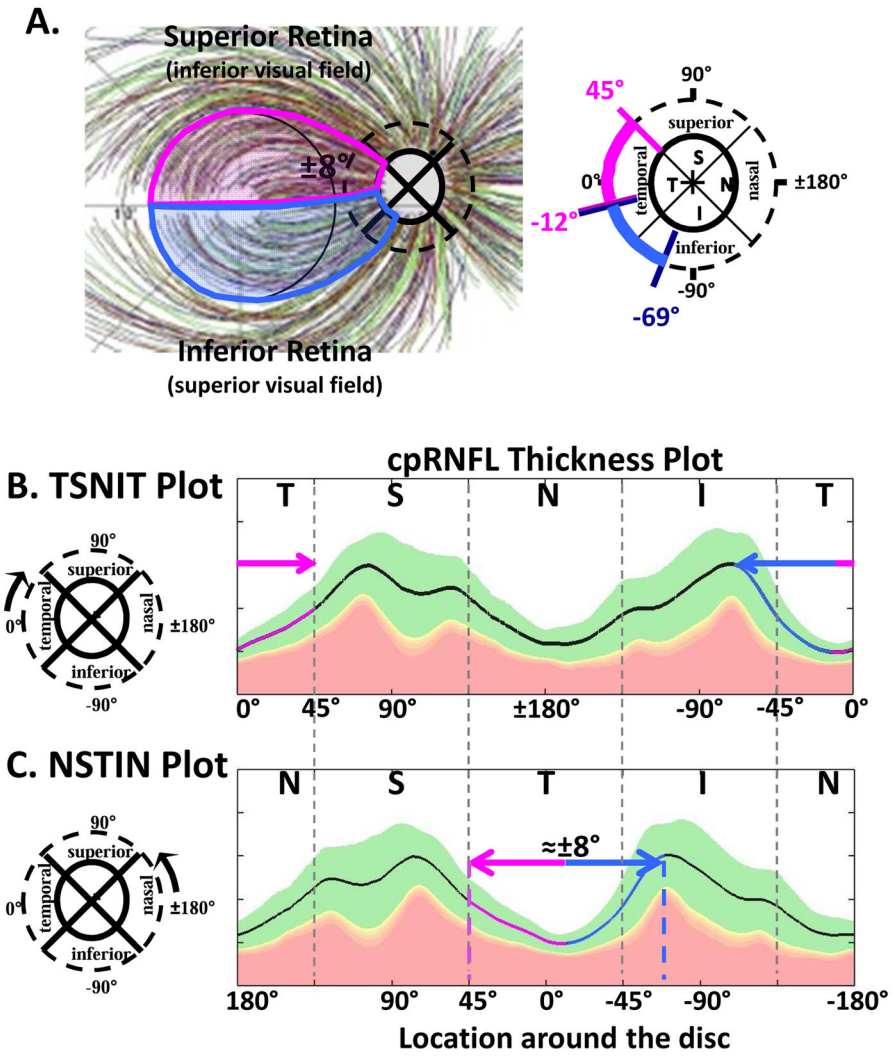

Fig. 1.

A schematic model of the macula relating retinal ganglion cell (RGCs) axons locations to circumpapillary retinal nerve fiber (cpRNFL) locations. (A) The borders of the superior (magenta) and inferior (light blue) regions of the macula supplying RNF input to the disc are superimposed on RNFL tracings modified from Fig. 2A in Jansonius et al. (2012), with permission. (B) The cpRNFL thickness plot is shown in the typical temporal (N) to superior (S) to nasal (N) to inferior (I) to temporal (N) orientation. The regions of the cpRNFL associated with macula (±8°) are shown by the magenta and light blue horizontal lines and arrows. (C) Same as (B) but with the cpRNFL thickness plot shown in the NSTIN orientation.

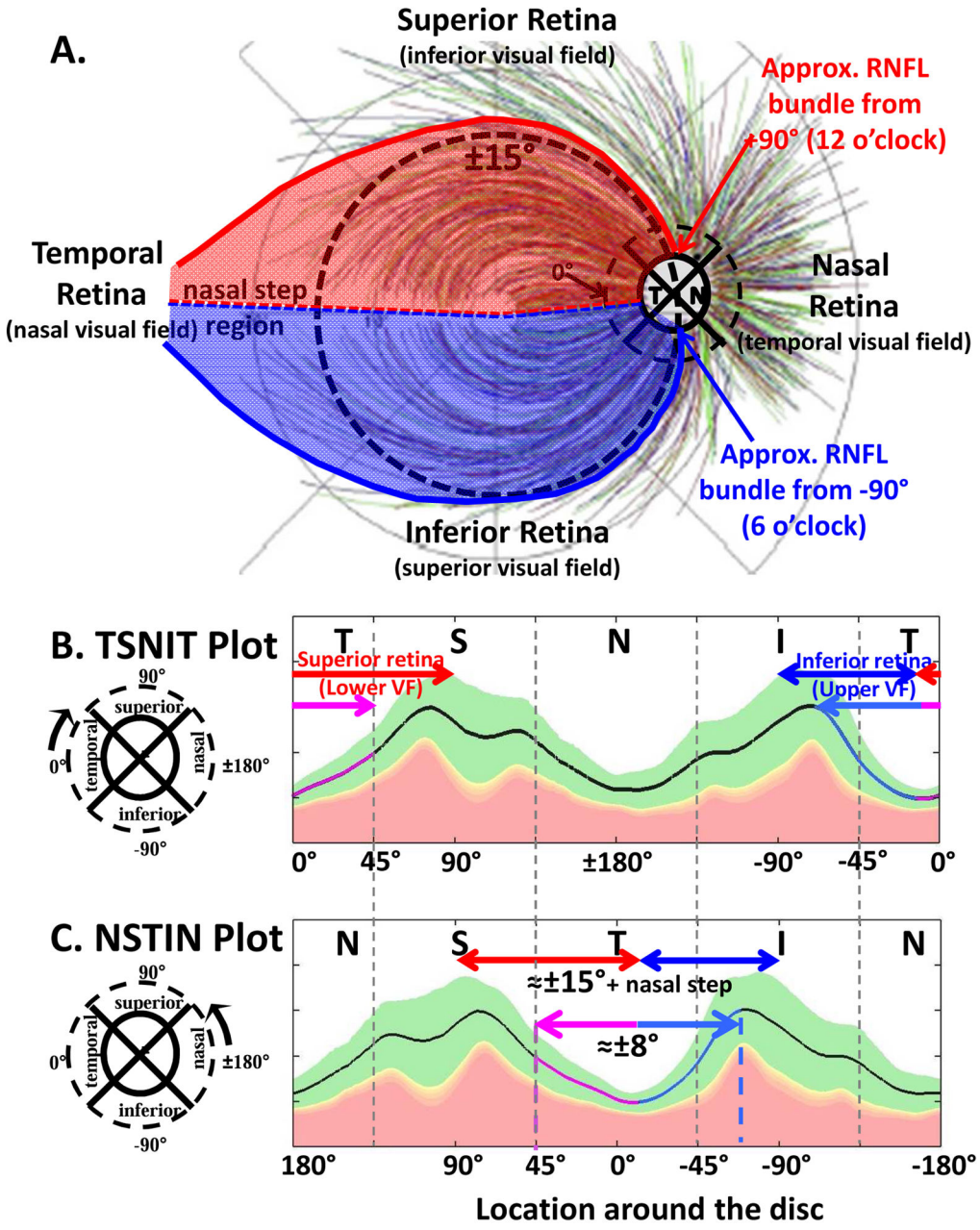

Fig. 2.

A schematic model relating RGC axons locations to cpRNFL locations of the temporal half of the disc. (A) The borders of the superior (red) and inferior (blue) regions of the retina supplying RNF input to the temporal half of the disc are superimposed on RNFL tracings modified from Fig. 2A in Jansonius et al. (2012), with permission. (B) The cpRNFL thickness plot is shown in the TSNIT orientation. The regions of the cpRNFL associated with the central retinal region (±15°+nasal step region) are shown by the red and blue horizontal lines and arrows. (C) Same as in panel (B) but the cpRNFL thickness plot shown in the NSTIN orientation.

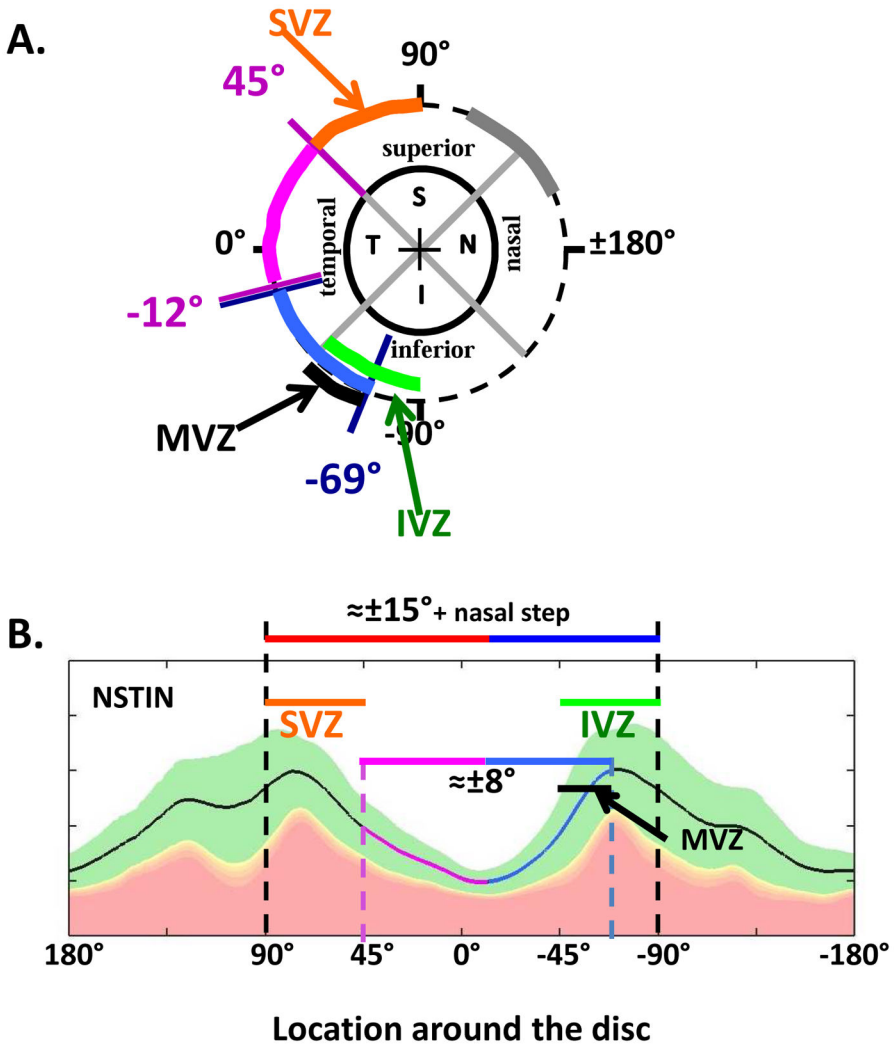

Fig. 3.

A schematic model showing the regions (orange, gray, and green) of the disc most vulnerable to local glaucomatous damage as reported by Hood et al. (2013b). (A) The temporal half of the disc has two vulnerable regions, the superior vulnerability zone (SVZ) and the inferior vulnerability zone (IVZ). The IVZ (green) overlaps the region of the cpRNFL (light blue) associated with the inferior macular retinal region. This region of overlap (black) is the macula vulnerability zone (MVZ). The SVZ (orange) does not overlap the region of the disc (magenta) associated with the superior macular retinal region. (B) The NSTIN cpRNFL thickness plot showing the regions around the disc associated with the temporal half of the disc (red and blue), with the macula (magenta and light blue), and the SVZ (orange), IVZ (green) and MVZ (black) indicated with horizontal lines.

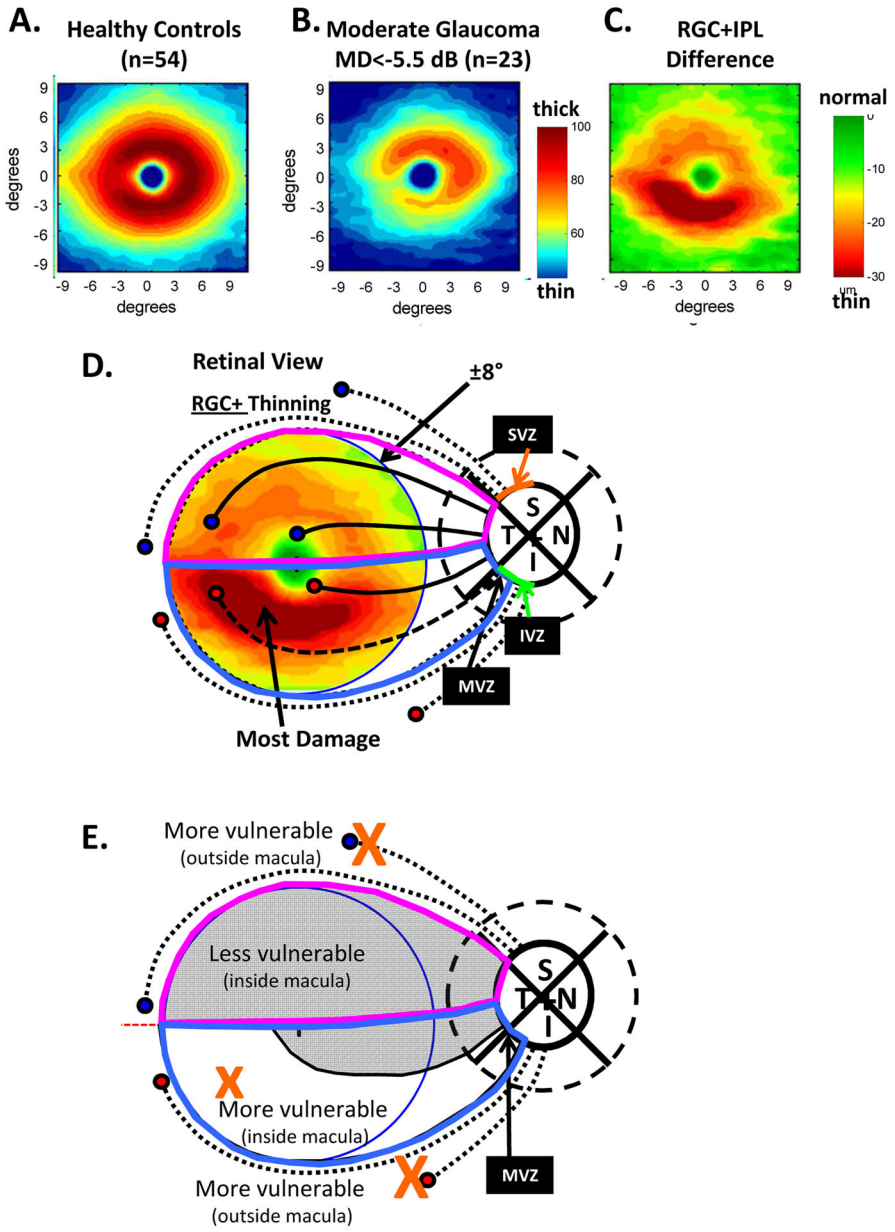

Fig. 4.

Retinal ganglion cell plus inner plexiform thickness (RGC+) and glaucomatous damage seen with spectral domain (sd) OCT. (A) The average RGC+ thickness map for 54 healthy controls shown in pseudo-color. (B) The average RGC+ thickness map for 23 patients with moderate glaucoma [i.e., 24-2 visual field mean deviation (MD) worse than −5.5 dB] shown in pseudo-color. (C) A difference map generated by subtracting the RGC+ thickness map for the age-similar controls in panel (A) from the RGC+ thickness map in panel (C). The color indicates the degree of thinning. (D) The schematic model of the macula from Figs. 1 and 3 is superimposed upon the central ±8° of panel C to indicate the relationship of the thinned region in panel C to the region projecting to the MVZ. The circles represent groups of RGCs and the associated black lines bundles of axons. The axon bundles with solid black lines feed

into the temporal quadrant, while those with the interrupted black lines project to the SVZ (upper dotted), the MVZ of the IVZ (dashed) and IVZ outside the MVZ (lower dotted). (E) The regions from panel D are shown with the more and less vulnerable regions labelled. Panels A, B and C are modified from (Hood et al., 2012).

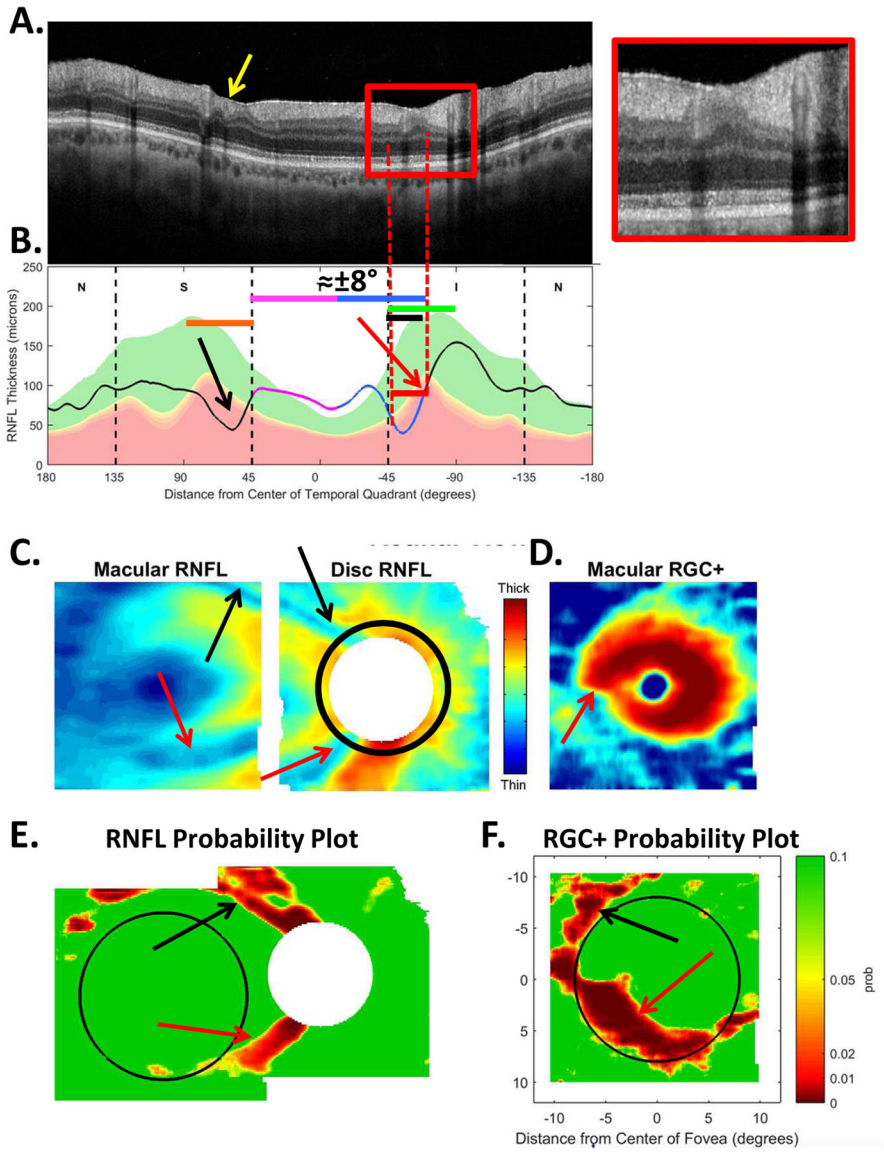

Fig. 5.

The sdOCT results for an eye with a relatively local, but relatively deep cpRNFL defect. (A) An image from a circumpapillary scan along with the region within the red rectangle showed enlarged to the right. The white arrows point to the defect. (B) The cpRNFL thickness plot (black, magenta, and light blue curve) obtained from the disc cube scan (solid) in panel (C, left panel) and the circle scan (dashed) in panel (A) and shown in NSTIN orientation as in Fig. 1C. (C) The RNFL thickness map from the sdOCT cube scan of the macula (left) and disc (right). (D) The RGC+ thickness map from the sdOCT cube scan of the macula. (E) The RNFL probability maps based upon the thickness maps in panel (C). (F) The RGC+ probability map based upon the thickness maps in panel (D). The black circles in panels (E) and (F) show the borders (±8°) of the macula. The arrows in all panels show the abnormal regions associated with the superior (black) and inferior (red) defects.

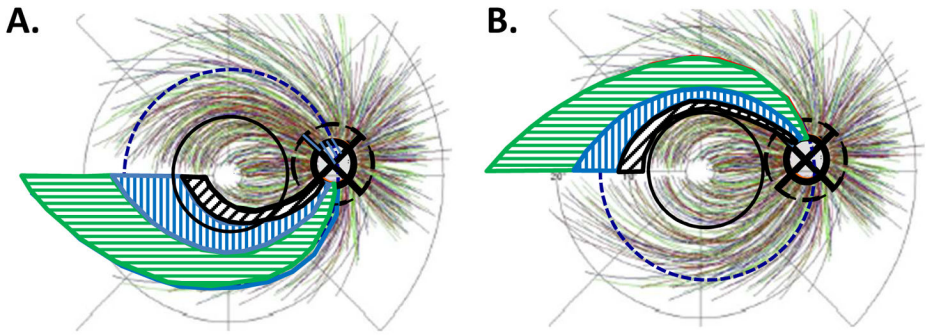

Fig. 6.

The retinal regions of 3 hypothetical deep cpRNRL defects of the IVZ (A) and SVZ (B). Each region is associated with a 15° segment of the IVZ or SVZ. These regions were approximated from the RNFL tracings of Jansonius et al (2012), shown as the faint tracings.

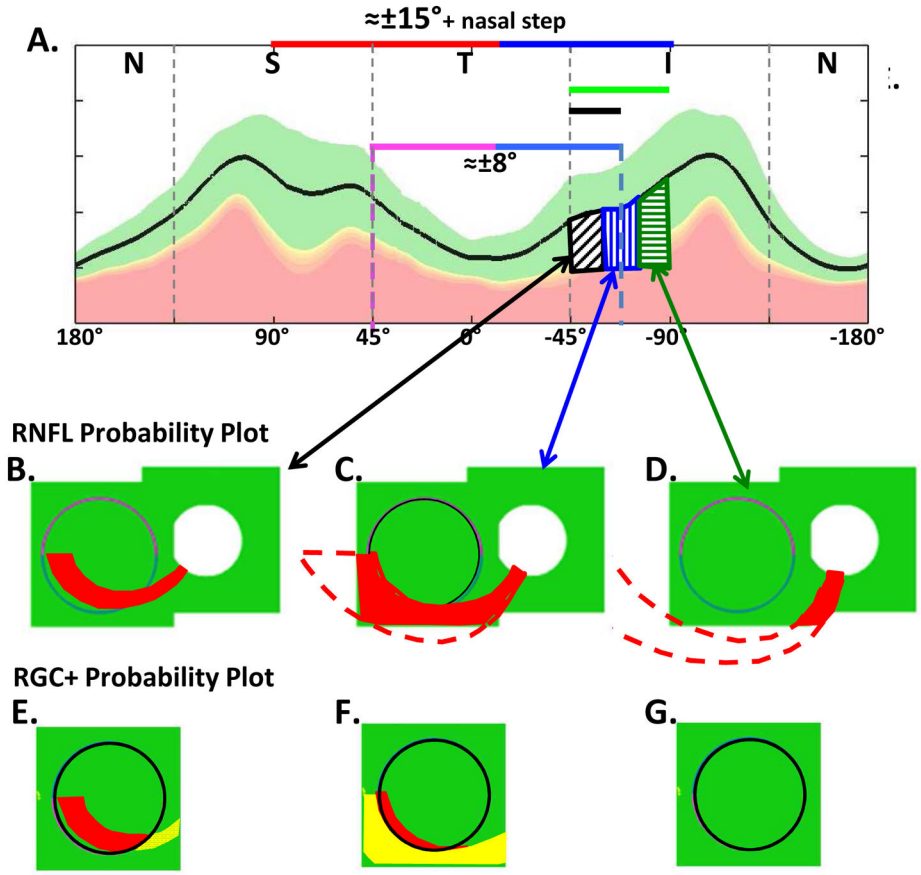

Fig. 7.

The RNFL and RGC+ probability maps predicted by the schematic model for 3 hypothetical IVZ defects that are relatively narrow, but deep. (A) A cpRNFL thickness plot as in Fig. 1C and 2C showing the location of 3 hypothetical defects (black, blue and green regions). (B) (C)(D) The predicted RNFL probability maps for the 3 defects. (E)(F)(G) The predicted RGC+ probability maps for the 3 defects. In panels (B–G), green and red indicate within normal limits and significantly abnormal, respectively, while yellow indicates a thinned RGC+ region that may or may not be obvious on the RGC+ plot as the RGC+ layer outside the macula (black circle) is relatively thin, even when healthy.

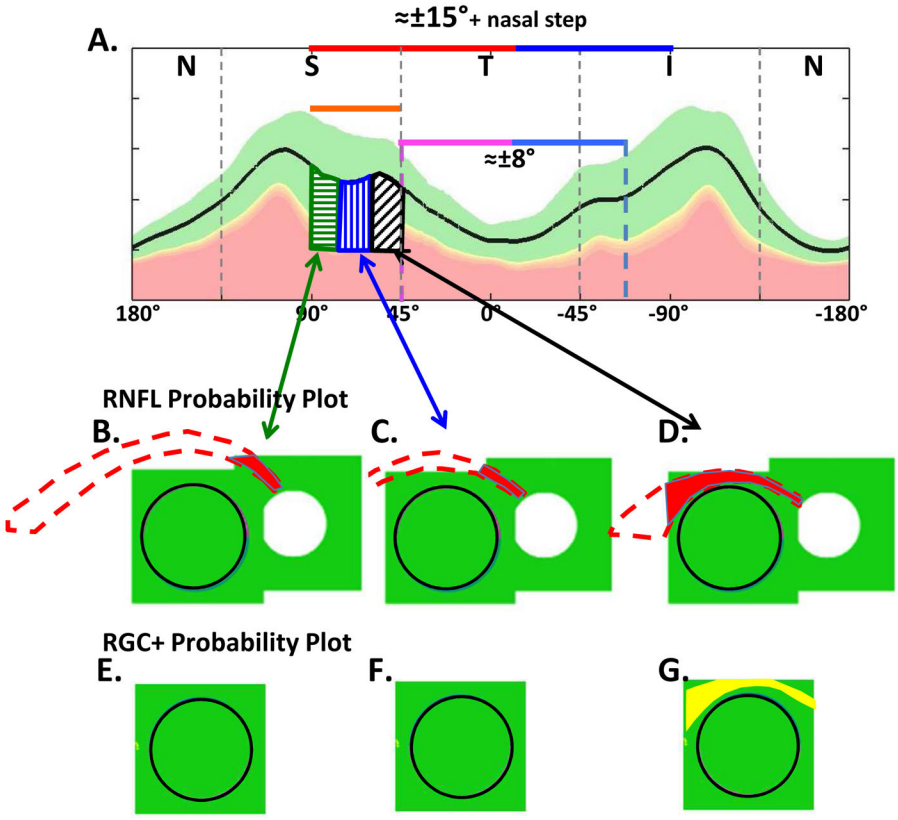

Fig. 8.

The RNFL and RGC+ probability maps predicted by the schematic model for 3 hypothetical SVZ defects that are relatively narrow, but deep. (A)–(G) Same as corresponding panels in Fig. 7, but for 3 hypothetical SVZ defects.

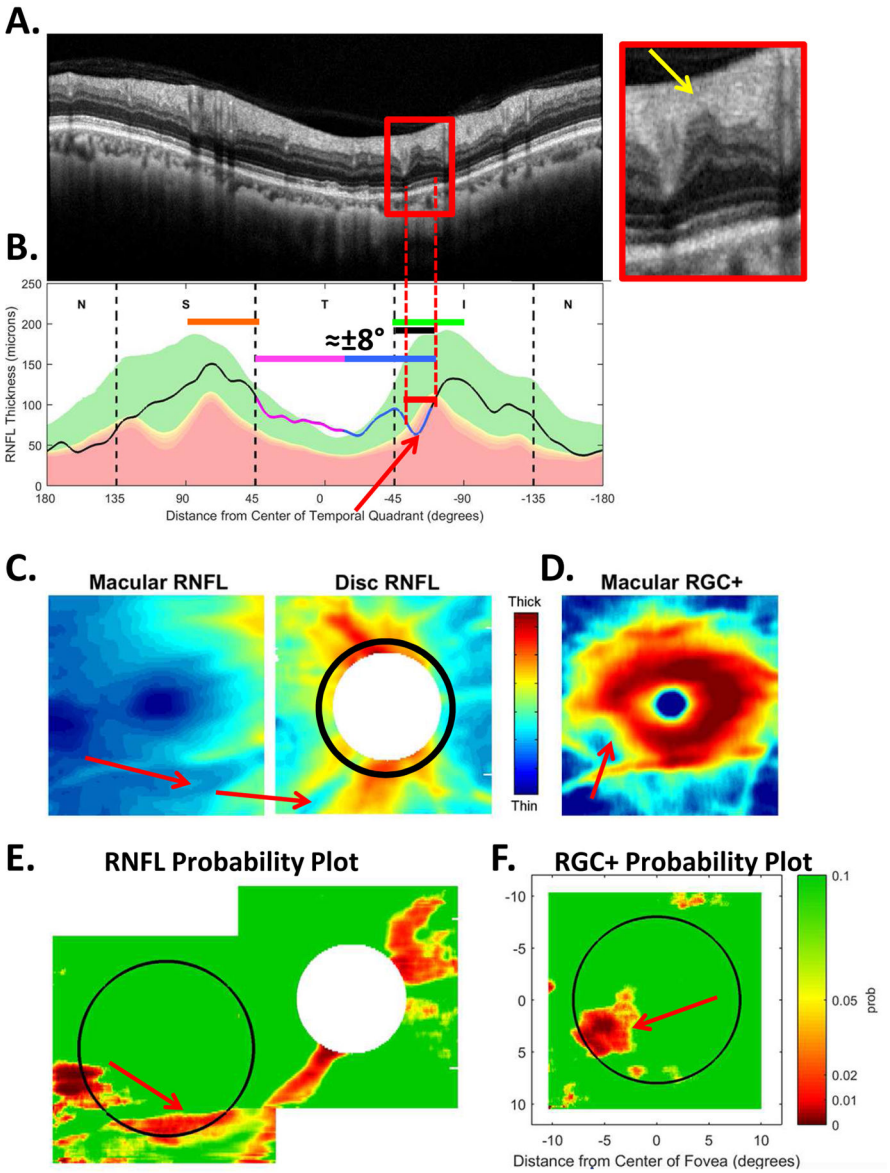

Fig. 9.

The sdOCT results for an eye with a relatively local and relatively shallow cpRNFL defect. (A)–(F) Same as corresponding panels in Fig. 5. The red arrows in all panels show the abnormal regions.

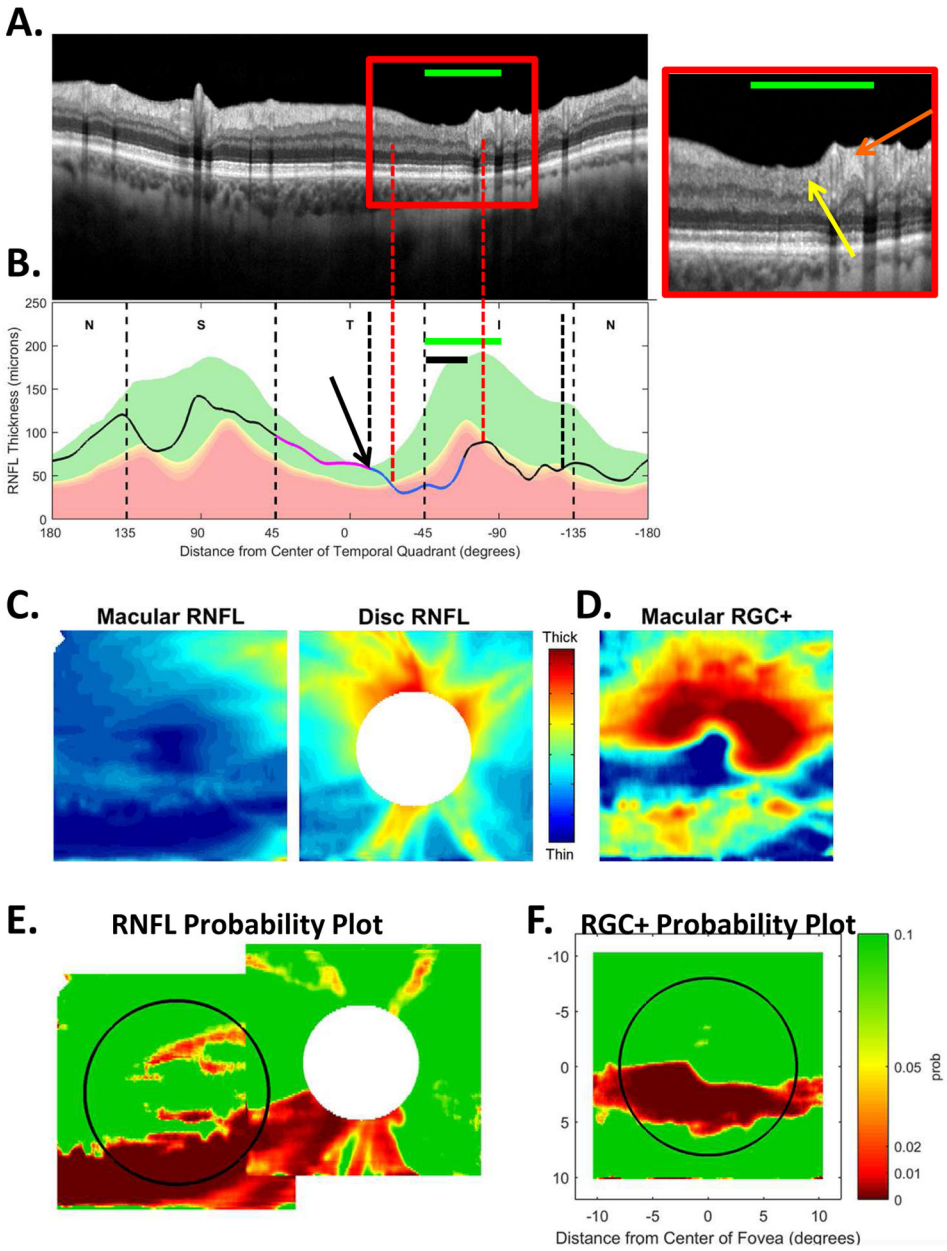

Fig. 10.

The sdOCT results for an eye with a relatively wide and relatively deep cpRNFL defect. (A)–(F) Same as corresponding panels in Fig. 5. In panel (A), the arrows point to locations of the defect with little or no RNFL remaining (white) and with some RNFL remaining (yellow). The green horizontal line indicates the extent of the IVZ in panels (A–C). In panel (B), the black arrow indicates the approximate point on the disc corresponding to the midline of the macula.

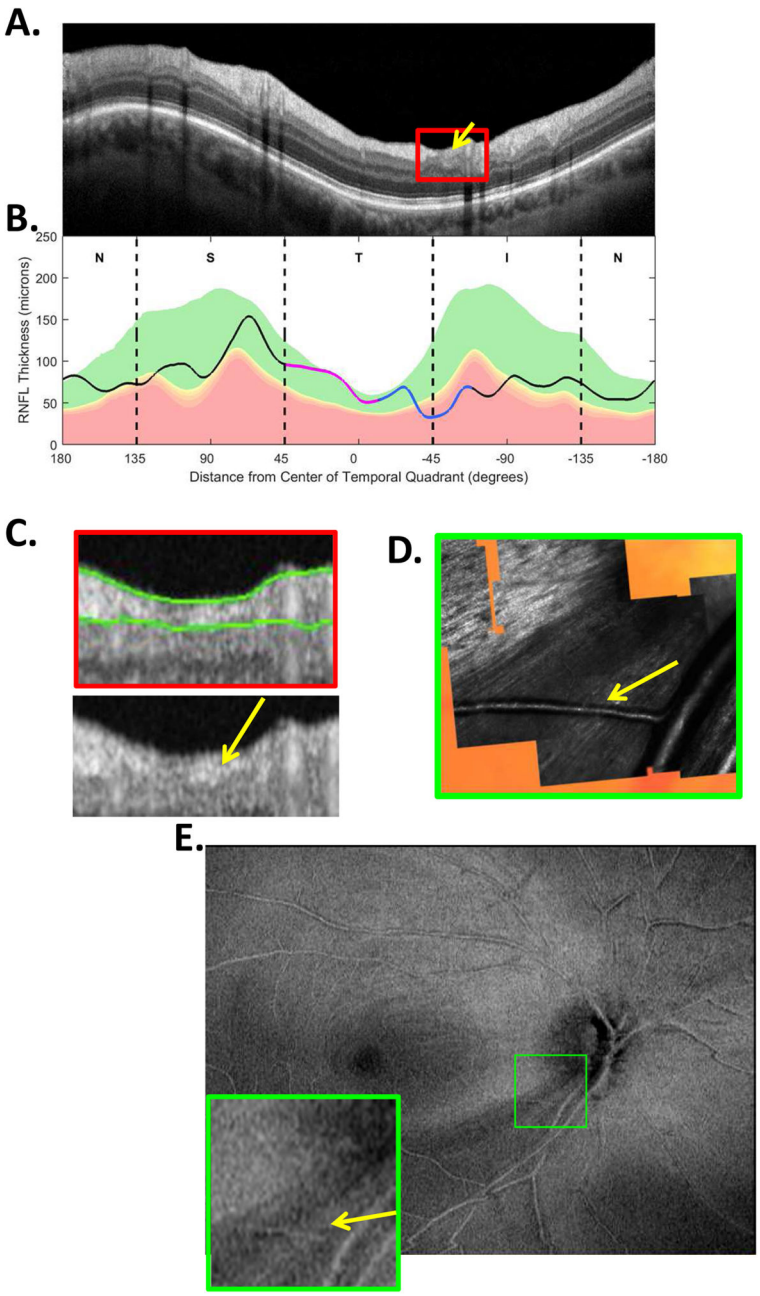

Fig. 11.

The sdOCT and AO-SLO results for an eye with a relatively wide and relatively heterogeneous cpRNFL defect. (A) An image from a circumpapillary scan. (B) The cpRNFL thickness plot (black, magenta, and light blue curve). (C) Enlarged view of the portion of the cpRNFL scan within the red rectangle in panel (A) shown with (upper) and without (lower) the segmentation of the cpRNFL shown. (D) An AO-SLO image. (E) An en-face image of a wide-field scan of this eye with the region within the green rectangle enlarged in the lower right corner. This region corresponds to the region within the AO-SLO image in panel D. The arrows in panels (C–E) correspond to the same locations with largely missing RNFL

bundles (white) and with some preservation of RNF bundles (yellow). Panels (D) and (E) are modified from Fig. 4A, B in Hood et al. (2015B).

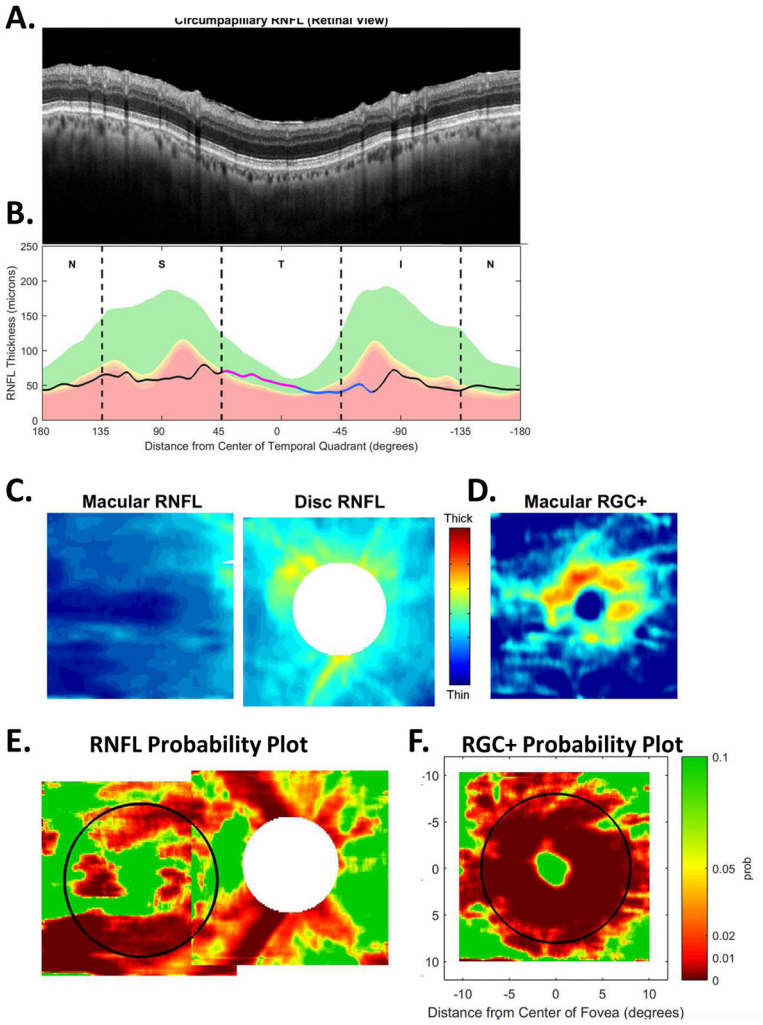

Fig. 12.

The sdOCT results for an eye with widespread cpRNFL damage. (A) An image from a circumpapillary scan. (B) The cpRNFL thickness plot (black, magenta, and light blue curve). (C) The RGC+ probability plot. (D) The RNFL probability plot.

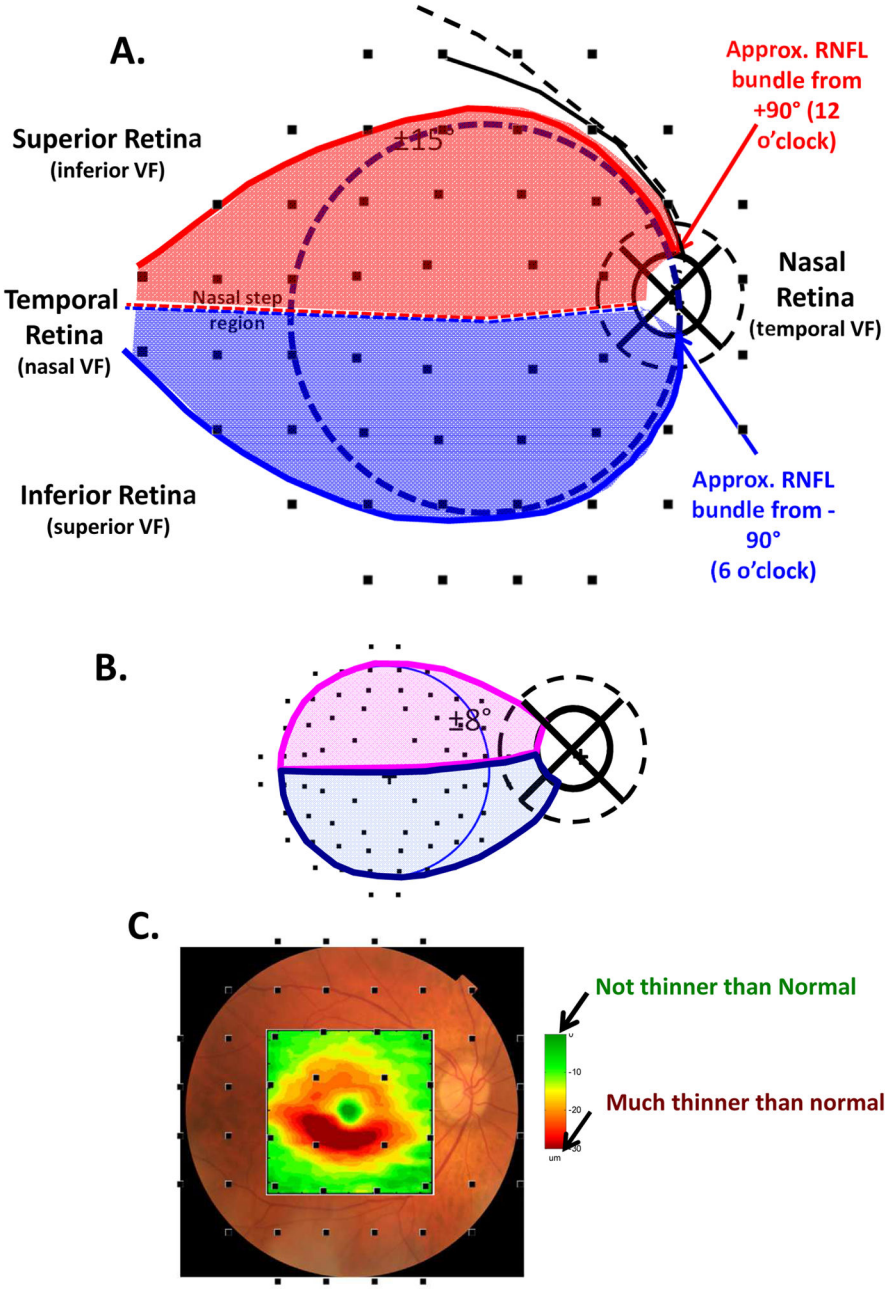

Fig. 13.

The schematic model with the location of the VF test points. (A) The schematic model from Fig. 2A with the location of the 24-2 VF test points. The solid black curve represents axons coming from RGCs in the region of one of the 24-2 VF test points, while the dashed black curve represents axons from from RGCs outside the 24-2 VF. (B) The schematic model from Fig. 1A with the location of the 10-2 VF test points. (C) A fundus view with the RGC+ thinning map from Fig. 5C along with the location of the 24-2 VF test points. In all panels, the VF locations are adjusted to account for the displacement of RGCs near the fovea (Hood et al, 2011). Panel C modified from Hood et al. (2013a).

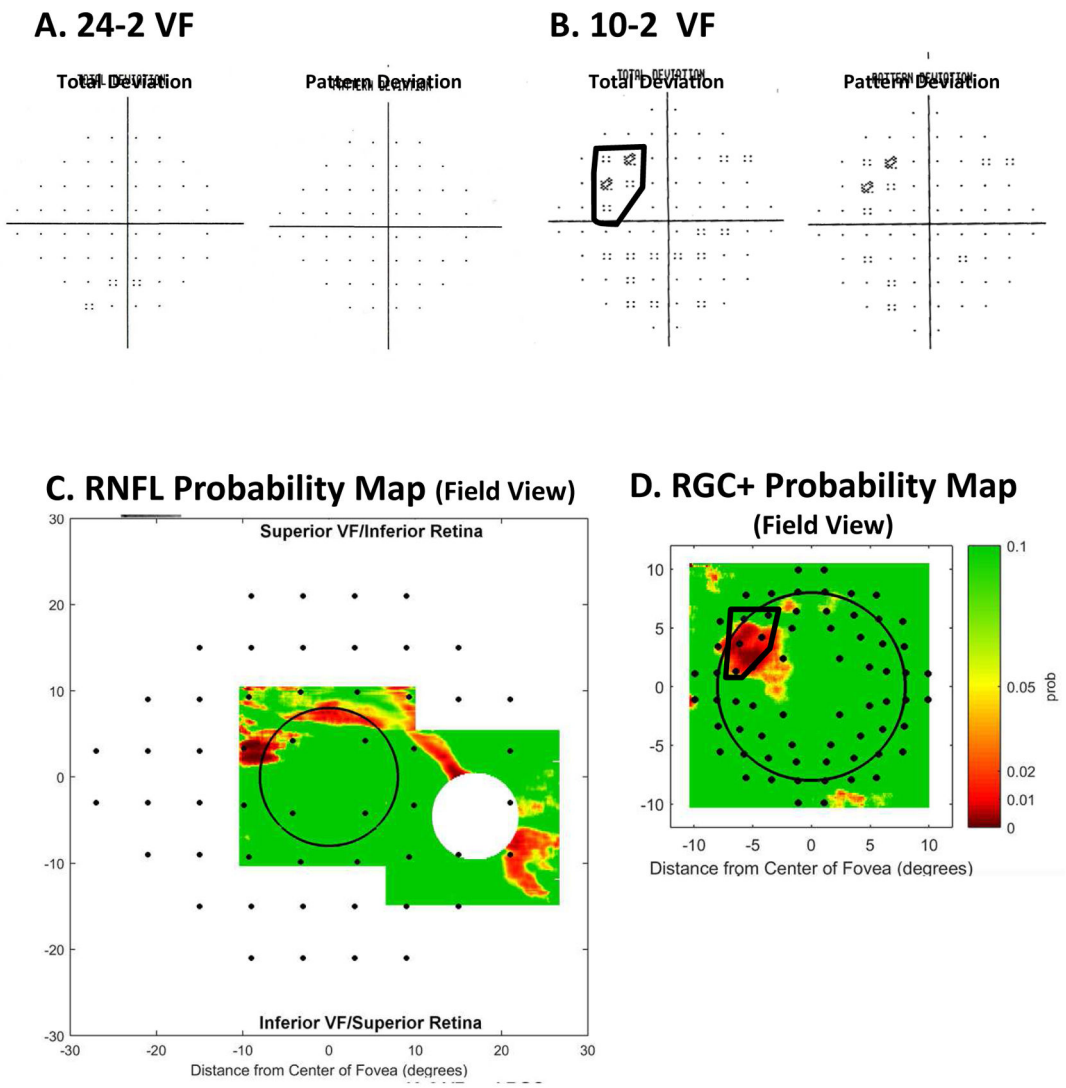

Fig. 14.

A comparison of abnormal regions on the VFs and OCT RNFL and RGC+ probability maps for the eye in Fig. 9. (A) 24-2 VF probability maps. (B) 10-2 VF probability maps with an abnormal region enclosed within the black border. (C) The RNFL probability map from Fig. 9E flipped to be in field view and with the 24-2 VF locations from Fig. 13A superimposed. (D) The RGC+ probability map from Fig. 9F flipped to be in field view with the 10-2 VF locations from Fig. 13B superimposed. The 10-2 points within the black border are the same as in panel (B).

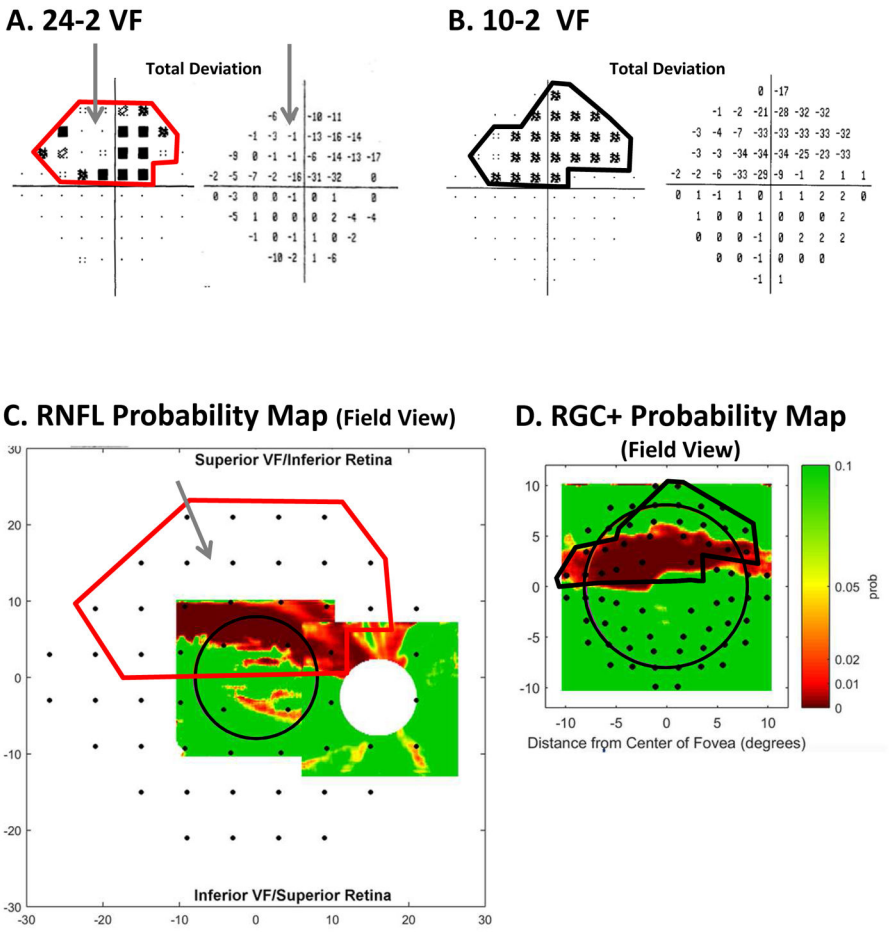

Fig. 15.

A comparison of abnormal regions on the VFs and OCT RNFL and RGC+ probability maps for the eye in Fig. 19. (A) 24-2 VF total deviation (TD) probability map (left) and TD values (right) with an abnormal region enclosed within the red border. The gray arrow indicates an area of the VF with relatively good TD values. (B) 10-2 VF total deviation (TD) probability map (left) and TD values (right) with an abnormal region enclosed within the black border. (C) The RNFL probability map from Fig. 10E flipped to be in field view and with the 24-2 VF locations from Fig. 13A superimposed. The 24-2 points within the red border are the same as in panel (B). (D) The RGC+ probability map from Fig. 10F flipped to be in field view with the 10-2 VF locations from Fig. 13B superimposed. The 10-2 points within the black border are the same as in panel (B).

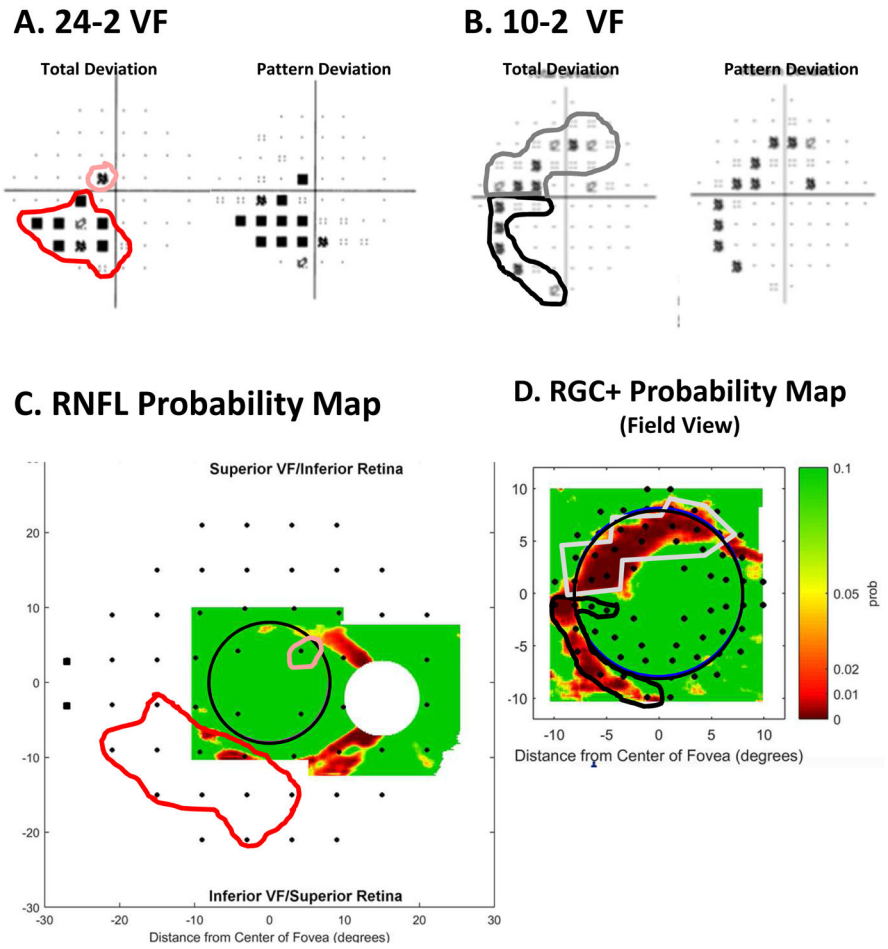

Fig. 16.

A comparison of abnormal regions on the VFs and OCT RNFL and RGC+ probability maps for the eye in Fig. 5. (A) 24-2 VF probability maps with abnormal regions enclosed within the pink (upper VF) and red (lower VF) borders. (B) 10-2 VF probability maps with an abnormal region enclosed within the gray (upper VF) and black (lower VF) borders. (C) The RNFL probability map from Fig. 5E flipped to be in field view and with the 24-2 VF locations from Fig. 13A superimposed. The 24-2 points within the pink and red borders are the same as in panel (A). (D) The RGC+ probability map from Fig. 5F flipped to be in field view with the 10-2 VF locations from Fig. 13B superimposed. The 10-2 points within the gray and black borders are the same as in panel (B).

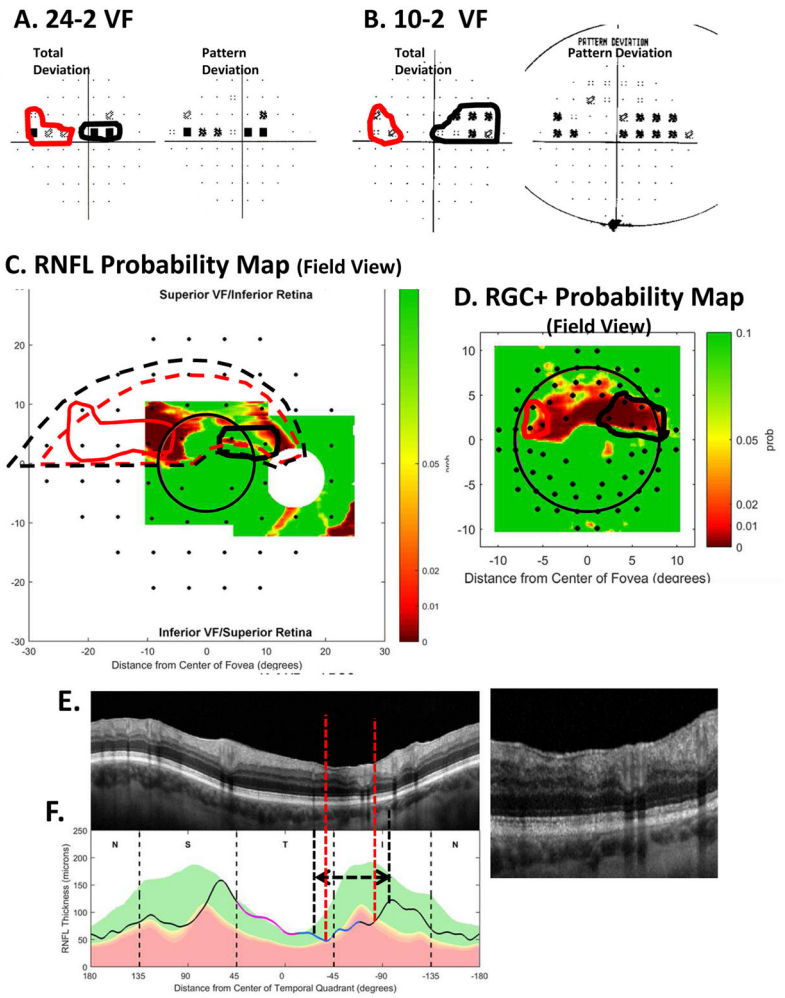

Fig. 17.

A comparison of abnormal regions on the VFs and OCT RNFL and RGC+ probability maps for an eye with an “atypical” VF pattern. (A) 24-2 VF probability maps with abnormal regions enclosed within the red and black borders. (B) 10-2 VF probability maps with an abnormal region enclosed within the red and black borders. (C) The RNFL probability map in VF view with the 24-2 VF locations from Fig. 13A superimposed. The 24-2 points within the red and black borders are the same as in panel (A). (D) The RGC+ probability in VF view with the 10-2 VF locations from Fig. 13B superimposed. The 10-2 points within the red and black borders are the same as in panel (B).

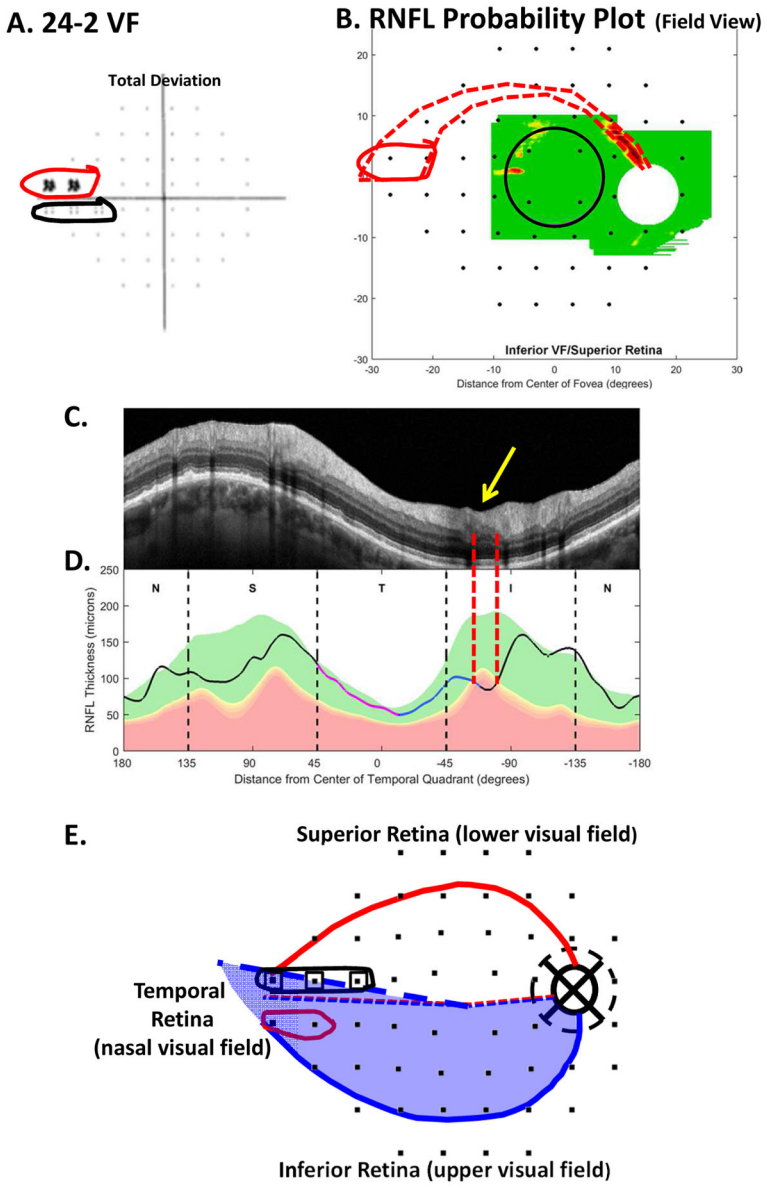

Fig. 18.

A comparison of abnormal regions on the VFs and OCT RNFL and RGC+ probability maps for an eye with nasal step defects. (A) 24-2 VF total deviation probability map with abnormal regions enclosed within the red and black borders. (B) The RNFL probability map in VF view with the 24-2 VF locations from Fig. 13A superimposed. The 24-2 points within the red borders are the same as in panel (A). (C) The circumpapillary scan for this eye with the corresponding abnormal cpRNFL region (yellow arrow) between the dashed red vertical lines. (D) The cpRNFL thickness plot for this eye. The abnormal region is between the dashed red vertical lines. (E) The model with 24-2 points from Fig. 13A with the regions of abnormal points from panel (A) enclosed within the black and red borders. The dashed bold blue line shows the location of the raphe in this eye.

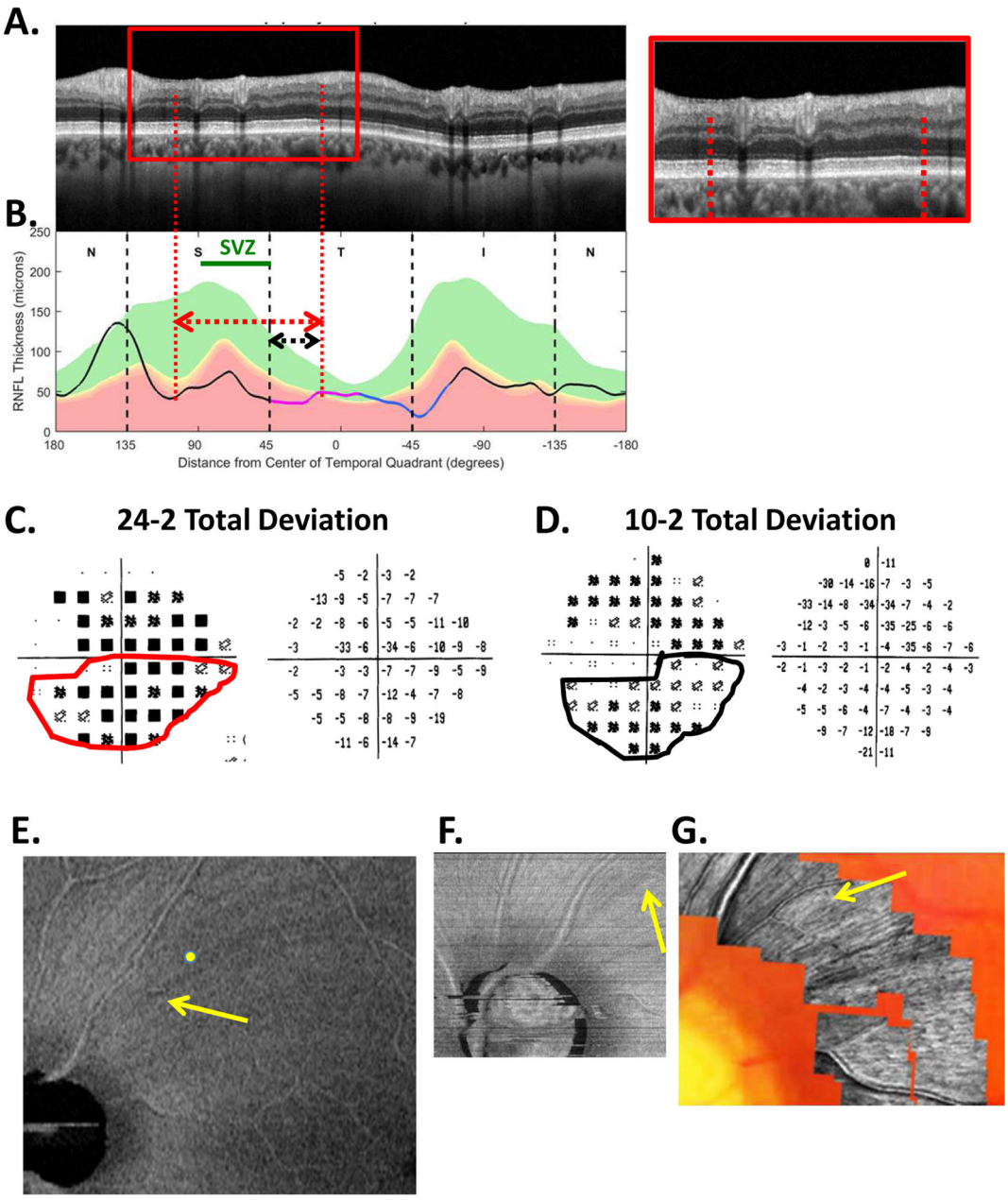

Fig. 19.

The sdOCT results for an eye with widespread cpRNFL damage. (A) An image from a circumpapillary scan. (B) The cpRNFL thickness plot (black, magenta, and light blue curve). The SVZ is shown as the green line. (C) The 24-2 VF total deviation (TD) probability map (left) and TD values (right) with the inferior abnormal region enclosed within the red border. (D)) The 10-2 VF total deviation (TD) probability map (left) and TD values (right) with the inferior abnormal region enclosed within the black border. The corresponding regions of the cpRNFL are indicated by the red and black lines with arrows in panels A and B. (E) An en-face slab image of the 9×12mm scan. (F) An en-face slab image of a 3×3mm scan of disc. (G) AO-SLO image. The yellow and white arrows are

approximately the same locations in panels (E), (F), and (G). Modified from Fig. 6A, B in Hood et al. (2015B).

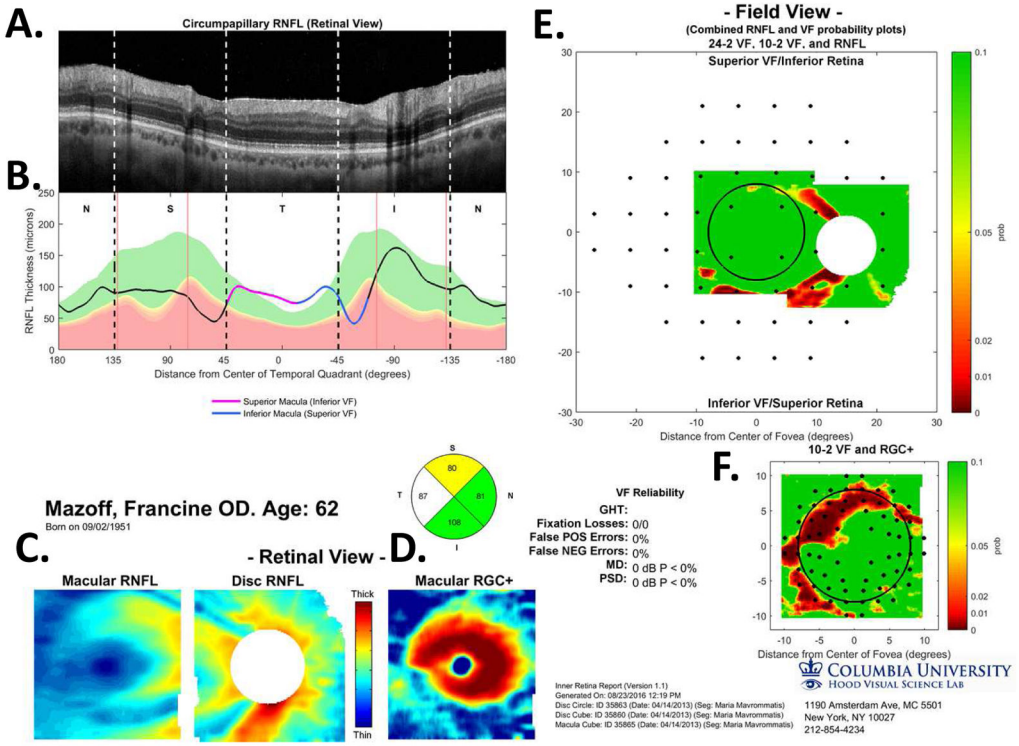

Fig. 20.

A one-page OCT report for the eye in Fig. 5. (A) An image from a circumpapillary scan. (B) The cpRNFL thickness plot (black) obtained from the disc cube scan (solid) in panel (C, left panel) and the circle scan (dashed) in panel (A) and shown in NSTIN orientation as in Fig. 1C. (C) The RNFL thickness map from the sdOCT cube scan of the macula (left) and disc (right). (D) The RGC+ thickness map from the sdOCT cube scan of the macula. (E) The RNFL probability maps based upon the thickness maps in panel (C) shown in VF view with the 24-2 VF locations from Fig. 13A superimposed. (F) The RGC+ probability map based upon the thickness maps in panel (D) with the 10-2 VF locations from Fig. 13B superimposed. The black circles in panels (E) and (F) show the borders (±8°) of the macula and, the color bar to the right shows the probability for both the OCT thickness. Designed by Hood and Raza (2014).

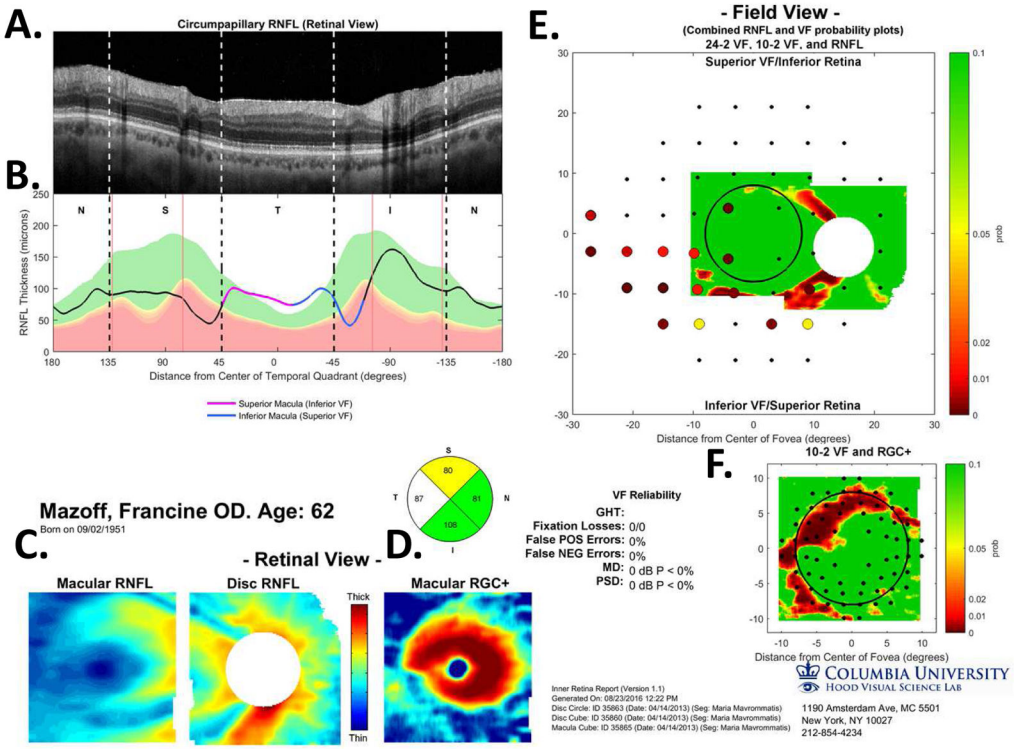

Fig. 21.

A one-page OCT report for the eye in Fig. 20 without VF probabilities.

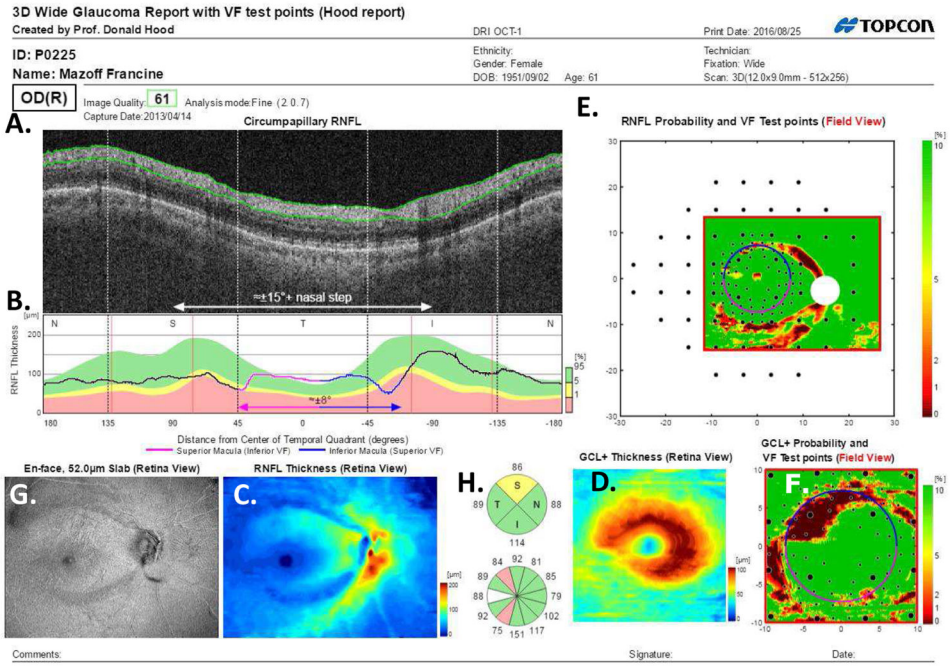

Fig. 22.

A one-page commercial report for the eye in Fig. 5 based upon a single wide-field (9×12mm) swept-source OCT cube scan [9.30beta (Atlantis) and v1.16beta (IMAGEnet6), Topcon Inc, Tokyo, Japan]. (A) An image derived from the wide-field scan. (B) The cpRNFL thickness plot (black) obtained from the disc cube scan and shown in NSTIN orientation as in Fig. 1C. (C) The RNFL thickness map from the sdOCT cube scan of the macula (left) and disc (right). (D) The RGC+ thickness map from the wide-field cube scan. (E) The RNFL probability maps based upon the thickness maps in panel (C) shown in VF view with the 24-2 and 10-2 VF locations from Fig. 13A.B superimposed. (F) The RGC+ probability map based upon the thickness maps in panel (D) with the 10-2 VF locations from Fig. 13B superimposed. The circles in panels (E) and (F) show the borders (±8°) of the macula and, the color bar to the right indicates the probability for the OCT thickness. G. An en-face slab image as described in Hood et al (2015b). (H) Pie charts showing the thickness values and probabilities for quadrants (top) and clock hours (bottom). Green, yellow and red indicate within normal limits, p≤0.05 and p≤0.01. See Hood et al (2016).

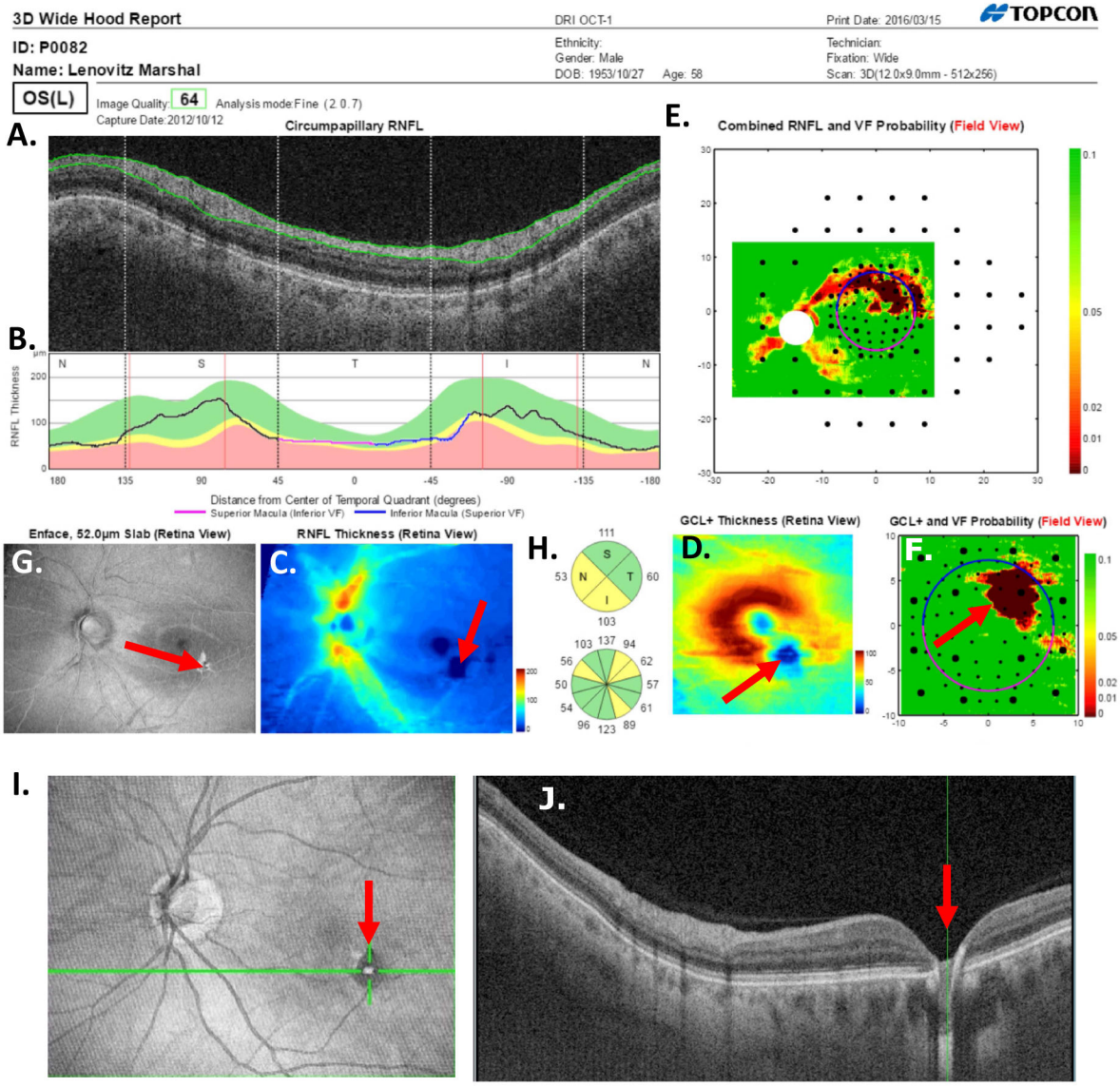

Fig. 23.

An eye with local damage of the RNFL and RGC+ layer due to a vitelliform macular detachment (VMD). (A)–(H) as in Fig. 22. (J) The b-scan (right) along the green line on the en-face image in panel I. The red arrow shows the same location in panels (C, D, G, I and J).

Table 1

False negatives (misses) and false positives of cpRNFL metrics.

OCT Metrics	Glaucoma misses *N=57*	"Healthy" false positives *N=45*	Accuracy *N=102*
Q	9 (15.8%)	4 (8.9%)	87.3%
CH	12 (21.1%)	2 (4.4%)	86.3%
T (<96.0 um)	10 (17.5%)	5 (11.1%)	85.3%
Any 1 of 3	8 (14.0%)	8 (17.8%)	84.3%